Antibody gene transfer treatment drastically improves epidermal pathology in a keratitis ichthyosis deafness syndrome model using male mice

Chiara Peres,[a] Caterina Sellitto,[b] Chiara Nardin,[a,g] Sabrina Putti,[a] Tiziana Orsini,[a] Chiara Di Pietro,[a] Daniela Marazziti,[a] Adriana Vitiello,[c] Arianna Calistri,[c] Mara Rigamonti,[d] Ferdinando Scavizzi,[a] Marcello Raspa,[a] Francesco Zonta,[e] Guang Yang,[e] Thomas W. White,[b,*] and Fabio Mammano[a,f,**]

[a]Institute of Biochemistry and Cell Biology, Italian National Research Council, 00015 Monterotondo, Rome, Italy
[b]Department of Physiology and Biophysics, Stony Brook University, T5-147, Basic Science Tower; Stony Brook, NY, 11794-8661, USA
[c]Department of Molecular Medicine, University of Padova, 35121, Padova, Italy
[d]Tecniplast SpA, 21020, Buguggiate, Italy
[e]Shanghai Institute for Advanced Immunochemical Studies, ShanghaiTech University, Shanghai, 201210, China
[f]Department of Physics and Astronomy "G. Galilei", University of Padova, 35131, Padova, Italy

eBioMedicine
2023;89: 104453
Published Online xxx
https://doi.org/10.1016/j.ebiom.2023.104453

Summary

Background Keratitis ichthyosis deafness (KID) syndrome is a rare disorder caused by hemichannel (HC) activating gain-of-function mutations in the *GJB2* gene encoding connexin (Cx) 26, for which there is no cure, or current treatments based upon the mechanism of disease causation.

Methods We applied Adeno Associated Virus (AAV) mediated mAb gene transfer (AAVmAb) to treat the epidermal features of KID syndrome with a well-characterized HC blocking antibody using male mice of a murine model that replicates the skin pathology of the human disease.

Findings We demonstrate that *in vivo* AAVmAb treatment significantly reduced the size and thickness of KID lesions, in addition to blocking activity of mutant HCs in the epidermis *in vivo*. We also show that AAVmAb treatment eliminated abnormal keratinocyte proliferation and enlarged cell size, decreased apoptosis, and restored the normal distribution of keratin expression.

Interpretation Our findings reinforce the critical role played by increased HC activity in the skin pathology associated with KID syndrome. They also underscore the clinical potential of anti-HC mAbs coupled with genetic based delivery systems for treating the underlying mechanistic basis of this disorder. Inhibition of HC activity is an ideal therapeutic target in KID syndrome, and the genetic delivery of mAbs targeted against mutant HCs could form the basis of new therapeutic interventions to treat this incurable disease.

Funding Fondazione Telethon grant GGP19148 and University of Padova grant Prot. BIRD187130 to FM; Foundation for Ichthyosis and Related Skin Types (FIRST) and National Institutes of Health grant EY 026911 to TWW.

Keywords: Genodermatosis; Connexin 26; Adeno-associated viral vectors; *In vivo* preclinical study

Introduction

Genodermatoses are inherited skin diseases that often present with multisystem involvement leading to increased morbidity and mortality.[1] Mutations in five Cx genes expressed in the epidermis (*GJA1, GJB2, GJB3, GJB4* and *GJB6*) can cause a variety of rare genodermatoses for which there is no cure, ranging in severity from mild increases in skin thickness to life-threatening and fatal barrier break down.[2] For these, as well as all other numerous Cx-related diseases, there is a compelling need to develop specific therapeutics.[3]

Increasing evidence points to leaky or hyperactive HCs as a common gain-of-function etiopathogenetic mechanism for a subgroup of Cx-related

*Corresponding author.
**Corresponding author.
E-mail addresses: thomas.white@stonybrook.edu (T.W. White), fabio.mammano@unipd.it (F. Mammano).
[g]Current address: Optical Approaches to Brain Function Laboratory, Istituto Italiano di Tecnologia; 16163, Genoa, Italy.

Research in context

Evidence before this study

Mutations in connexin26 (Cx26, or GJB2) that increase hemichannel activity underlie skin diseases that include keratitis-ichthyosis-deafness syndrome (KID). For diseases like KID syndrome, there is no cure, there are limited options for palliation, and the combined impact of hearing loss, disfigurement, and blindness greatly diminishes the quality of life for the affected individuals who survive infancy. Cx26 mutations causing KID syndrome induce increased hemichannel activity as their main functional change, and specific monoclonal antibodies have been developed to block this acquired activity.

Added value of this study

In this study, we have shown that the epidermal pathology can be alleviated in a mouse model that replicates the skin disease associated with human KID syndrome by systemic administration of a monoclonal antibody that blocks connexin hemichannels.

Implications of all the available evidence

These results confirm the hypothesis that increased hemichannel activity is a significant contributor to epidermal pathology in KID syndrome, and further show the potential use of specific monoclonal antibodies to inhibit hemichannel activity as a new therapeutic intervention to treat this disease. Since hemichannel dysfunction contributes to disease mechanisms in additional connexinopathies beyond KID syndrome, these findings could have broad impact for treating other hemichannel-dependent human disorders.

genodermatoses with autosomal dominant inheritance and an overlapping spectrum of cutaneous clinical features, which may drastically compromise quality of life and life-long health.[4–6] HCs are large pore hexameric structures that, when inserted in the cell plasma membrane, may selectively open to exchange inorganic cations and anions, as well as larger metabolites and signalling molecules between the cytoplasm and the extracellular milieu.[7,8] Bidirectional fluxes activated by the unregulated opening of HCs may deeply affect cytosol composition and cell viability.[4] In particular, the Cx26 (*GJB2*) variants p.G12R, p.N14K, p.N14Y, p.A40V, p.G45E, p.D50A, p.D50N and p.A88V generate leaky HCs that have been causally linked to KID syndrome (OMIM #148210)[9–21]; reviewed in.[22]

In general, the prognosis for KID syndrome is variable, with patients suffering from blindness, deafness, and disfigurement.[23] Skin abnormalities include unusually thick skin on the palms of the hands and soles of the feet (palmoplantar keratoderma), thick, red patches of skin (erythrokeratoderma), and dry, scaly skin (ichthyosis). Ichthyotic skin has decreased barrier function and a propensity for trans-epidermal water loss and infections. Eye problems are caused by keratitis (corneal inflammation) which can lead to pain, sensitivity to light, extra blood vessel growth, scarring, and eventual vision loss. KID syndrome can also lead to an aggressive form of squamous cell carcinoma.[23,24] The KID syndrome variants p.G45E and p.A88V of Cx26 have been shown to result in 100% lethality in infancy/early childhood.[25–30]

The overall goal of this study was to test the feasibility of a treatment for KID syndrome based on abEC1.1, an antagonist mAb targeting the extracellular domain of Cx HCs that has been a previously characterized and validated both *in vitro* and *in vivo*.[31–33] abEC1.1 and other mAbs are promising drug candidates for the treatment of genodermatoses.[34–37] Seminal work in mice treated with a recombinant mAb-encoding adeno-associated virus (AAV) vector showed sustained mAb levels in the circulation, using the AAV8 serotype that efficiently transduces the liver.[38] This procedure, known as antibody gene transfer, allows direct antibody production and secretion within the body that necessitates treatment.[39,40]

In the current study, we developed an antibody gene transfer approach for abEC1.1 and tested it in Cx26G45E mice (MGI:5635532), a well characterized inducible mouse model of KID syndrome.[2,41,42] Conditional expression of the p.G45E variant (and downstream EGFP) in the epidermis of heterozygous transgenic Cx26G45E mice leads to development of skin abnormalities within a few days of induction with doxycycline (dox), and epidermal pathology worsens progressively when mice are maintained on dox for longer periods. Histopathology shows papillomatosis and acanthosis, increased cell size and osteo-obstruction, increased apoptosis occurring primarily in the dermis and increased cell proliferation in the epidermis, related to increased HC currents measured by patch clamp in primary keratinocytes isolated from Cx26G45E mice.[2,41,42] We found that *in vivo* AAVmAb treatment with abEC1.1 reduced all of these features of the epidermal pathology in this mouse model.

Methods

Study design

The experimental unit for the present study was a single animal. The objectives of our study were (i) to determine whether caudal vein injection of an AAVmAb in the Cx26G45E mouse model of KID syndrome achieved therapeutic levels of abEC1.1 in the circulation, (ii) to characterize the therapeutic effect of the mAb on skin

pathology in this mouse model, and (iii) to assess the effect of the *in vivo* produced mAb on Cx HCs. The first objective relied on quantification of abEC1.1 serum concentration by ELISA (n = 18). The second objective required a multifaced analysis based on *in vivo* imaging of lesional skin area, skin histopathology and confocal immunofluorescence imaging with a variety of markers (n = 30). The third objective required an *in vivo* DAPI uptake assay (n = 15) and locomotion analysis (n = 12). Sample sizes were determined based on pilot studies to achieve 80% statistical power with a 95% confidence interval. Mice for these studies were randomly assigned to control and treatment groups (as described in the Results) by using the random number generator [X = rand(n)] of Matlab (R2019a, The MathWorks, Inc., Natick, MA, USA). To minimise potential confounders, the order of treatments and measurements, as well as cage location were also randomized in the same way. Experimenters were unblinded to group assignment and outcome assessment, for all experiments.

Animals

Mice were caged individually and bred under controlled pathogen-free conditions at the National Research Council–Institute of Biochemistry and Cell Biology (CNR-IBBC), Infrafrontier/ESFRI-European Mouse Mutant Archive (EMMA), Monterotondo, Rome, Italy. For all experiments on animals, we used Cx26-G45E double transgenic mice (MGI:5635532).[41] When a doxycycline (dox) containing diet is administered (625 mg/kg, Mucedola, Settimo Milanese, Italy), these mice express the mutant p.G45E of Cx26 and EGFP as independent proteins in epidermal keratinocytes. Animals were genotyped by PCR amplification of tail genomic DNA as previously described.[41] TheCx26G45E mouse model is characterized by a large phenotypic viability, such that only about 3% of the bred animals can be used for experiments, as reported previously.[42] Accordingly, more than 400 mice had to be screened over a 3-year period to achieve the cohorts with similar disease progression used for the present experimental studies. The limited sample size presented does not reflect this huge screening effort. During the screening process aimed at isolating animals with similar disease progression, we noted that female mice showed a significantly milder epidermal expression of pathological lesions. This is probably related to our mating strategy. For this reason, only adult male mice, aged between 5 and 17 weeks, were used for experiments. Weight data are provided in the Supplementary Material. The total number of mice, including breeders, used for this study was n = 1681.

Ethics

All animal procedures were agreed upon, reviewed and approved by local animal welfare oversight bodies and were performed with the approval and direct supervision of the CNR-IBBC/Infrafrontier – Animal Welfare and Ethical Review Body (AWERB), in accordance with general guidelines regarding animal experimentation, approved by the Italian Ministry of Health, in compliance with the Legislative Decree 26/2014 (ref. Project license 603/2018-PR and 632/2019-PR), transposing the 2010/63/EU Directive on protection of animals used in research) and in adherence to the NIH Guide for the Care and Use of Laboratory Animals and recommendations from both ARRIVE and PREPARE guidelines.[43,44]

mAb and AAVmAb production

The abEC1.1 mAb was isolated and produced as previously described.[31] Briefly, we first selected Cx-binding human antibody fragments by screening a vast library expressed in phage[45] with a bait peptide (pepEC1.1 = KEVWGDEQADFVCNTL). The selected fragments comprised a heavy chain variable domain (V_H) and a light chain variable domain (V_L) connected by a 7 a.a. flexible spacer to create a scFv complex (Protein Data Bank accession code 5WYM). Next, we formed abEC1.1 by cloning the coding sequence of the Cx-binding scFv in the pFUSE-mIgG1-Fc2 expression vector (4187 bp, Cat. No. pfuse-mg1fc2, InvivoGen, San Diego, CA, USA). Purified scFv-Fc polypeptides formed homodimers with a MW of ~103 kDa (the abEC1.1 proper)[31] through a diabody interaction between V_H and V_L[46] and disulphide bonds in the hinge region.[47] Purified abEC1.1 mAbs were used to construct ELISA standard curves as described below.

AAV2 inverted terminal repeats (ITRs)[48] were used in the custom-made (Project Tracking No. T200422-1004wrt, Vector Builder, Chicago, IL, USA) vector plasmid (pAAV [Exp]-CAG>[CodOpt-abEC1.1-mFc]:WPRE (VB200421-1436tku), Vector Builder, Fig. S1). Virions with an AAV8 capsid[38] were produced at a concentration of 6.24 $\times 10^{13}$ genome copies/ml (Cat. No. AAV8LP(VB200421-1436tku)-C, AAV8 virus large-scale packaging and ultra-purification service for pAAV[Exp]-CAG>[CodOpt-abEC1.1-mFc]:WPRE (VB200421-1436tku), Vector Builder), shipped on dry ice and used within one year from production. The ITR sequence of AAV2 was used as a target to quantify the amount of viral genome by quantitative polymerase chain reaction (qPCR) after extracting viral DNA from viral particles.

In vivo AAVmAb treatment

Cx26G45E double transgenic mice (35–40 days of age) with comparable level of pathology expression were partitioned into three different experimental groups: control (–dox), untreated (+dox) and treated (+dox + AAVmAb); each group comprised n = 6 males. Each + dox + AAVmAb animal was injected into the caudal vein with 120 µl of phosphate buffered saline solution (PBS) containing 1.25 × 10^{12} virus genome copies. Untreated –dox and +dox mice were injected with 120 µl of PBS alone (vehicle). +dox and +dox + AAVmAb

animals were induced with dox three weeks after AAV-mAb injection and imaged at 0, 3, 7, 11, 14, 17, 21, 28 days after induction. Age-matched –dox animals (not induced with dox) were imaged in parallel. At the end of the 4-week observation period, all mice were deeply anesthetized and euthanized with carbon dioxide for tissue harvesting and *ex vivo* analyses. The sacrifice was performed according to the law, without suffering for the animal.

Quantification of circulating mAb levels by ELISA

The biotinylated pepEC1.1 bait peptide that binds abEC1.1[31] (produced and lyophilized by Genosphere Biotechnologies, Paris, France) was diluted in a solution of PBS containing 0.1% Tween 20 (Cat. No. P1379, Sigma–Aldrich, St. Louis, MO, U.S.A). Streptavidin-coated ninety-six-well ELISA plates (Cat. No. MG0STF-SA5/200 Biomat, Ala, Italy) were incubated at room temperature (RT) for 30 min with 100 µl/well of this solution (equivalent to 0.1 µg/well of peptide). Plates were then washed three times with 200 µl/well of PBST buffer (0.005% Tween 20 in PBS).

To construct an ELISA standard curve,[49] the purified abEC1.1 mAb at the maximum concentration of 10 µg/ml in PBS buffer was diluted stepwise, by a 2^n factor in PBS, down to a minimum concentration of 0.15 µg/ml. 100 µl of each diluted abEC1.1 solution was added in triplicate and incubated for 2 h at 37 °C. Plates were then washed three times with PBST buffer and incubated with 100 µl/well of Goat Anti-Mouse peroxidase-conjugated secondary antibody (Cat. No. 115-035-071, Jackson Immuno-Research, Ely, Cambridgeshire, UK) diluted 1:5000 in diluent for HRP solution (Cat. No. 400-2, Biomat) at RT for 30 min. Plates were washed again 3 times with PBST, thereafter 100 µl/well of chromogen substrate (TMB, Cat. No. 002023, Thermo-Fisher Scientific, Waltham, MA, USA) was added and plates were incubated at RT for 15 min. Finally, 100 µl/well of stop solution for TMB substrate (Cat. No. 600-1, Biomat) was added and the absorbance at 450 nm was read out immediately with a plate reader (Varioskan LUX, Cat. No. N16045, Thermo-Fisher Scientific). The relationship established between absorbance and the known antibody concentration provided the standard curve.

To quantify antibody concentration in blood serum following AAVmAb or LVmAB administration, based on the ELISA standard curve, blood samples (≥200 µl) were withdrawn from the mouse caudal vein and transferred to 1.5 ml tubes and maintained for 1 h at RT to promote phase separation. Tubes were centrifuged at 12,000 rpm at RT for 5 min. The supernatant serum was transferred to fresh 1.5 ml tubes and stored at –20 °C. After thawing and proper dilution in PBS, the amount of antibody in mouse serum samples was quantified by ELISA, according to absorbance at 450 nm and standard curve, as described above for purified antibody samples.

All + AAVmAb animals included in this study had serum concentration sampled at weeks 3 and 8 after infection. Animals with abEC1.1 serum concentration below 35 µM at any one of these two time points were excluded from this study ($n = 3$). For measurements of serum antibody concentration, $n = 12$ animals were injected and divided into two groups of $n = 6$ mice per group to perform blood withdrawal every other week after viral infection; the first group was sampled on weeks 1,3,5,7,9, second group on weeks 2,4,6,8,10.

Lentiviral production and administration

For LVmAb production, a third generation self-inactivating HIV-derived lentiviral backbone vector (kindly provided by L. Naldini, Università Vita e Salute San Raffaele, Milan, Italy),[50] was used to clone abEC1.1 under the transcriptional control of the human cytomegalovirus (HCMV) promoter using BamHI and SalI restriction enzymes. Recombinant plasmids were verified by enzymatic restriction and correct clones were further confirmed by Sanger sequencing. The generated lentiviral vector DNAs were co-transfected along with the packaging plasmids pMDL, pVSV-G, and pRSV-Rev (a gift of L. Naldini) in 293T cells, by adopting calcium phosphate reagents. Forty-eight hours post-transfection, cell supernatants containing the recombinant lentiviral particles (RLPs) were harvested, filtered with a 0.45 µm-pore-size membrane (Millipore, Bedford, MA, USA), and concentrated 100 times by ultracentrifugation (27,000 rpm, 2 h, 4 °C in a Beckman SW28 rotor), or by adopting VivaSpin columns (Sartorius, Goettingen, Germany). RLPs expressing abEC1.1 were quantified by measuring the amount of the HIV-1 capsid p24 protein by ELISA assay (Cat. No. XB-1000, XpressBio, Frederick, MD, USA). Titer of RLPs was then expressed in transducing units (TU)/ml by converting the obtained pg of p24 per ml into TU/ml, following the manufacturer's instructions. For LVmAb treatment, mice at 35–40 days of age were injected into the caudal vein with 120 µl of PBS containing 2.96×10^6 LVmAb transducing units (TUs). Blood withdrawals were performed every other week and serum antibody concentration was estimated with ELISA as described above.

In vivo imaging of lesional skin area

For these experiments, we developed a dedicated system based on ratiometric reflectance imaging. The system comprised a gaseous anaesthesia apparatus and a feedback-controlled heating pad for homeothermic regulation of mouse body temperature (Fig. S2). The illumination source was a warm white light emitting diode (Cat. No. MWWHF2, Thorlabs Inc., Newton, NJ, USA) coupled to a multimode fibre (Ø1000 µm, Cat. No. M35L02, Thorlabs). We positioned the fibre output so as to uniformly illuminate the mouse back skin. Images of illuminated samples were collected by a digital camera with a cMOS colour sensor (Cat. No. DCC1645C,

Solution	Substance(s) dissolved in Ca^{2+}-free PBS
1	EGTA (5 mM)
2	EGTA (5 mM), DAPI (10 μM), Dex.TR (1.78 μM)
3	EGTA (5 mM), FFA (400 μM)
4	EGTA (5 mM), FFA (400 μM), DAPI (10 μM), Dex.TR (1.78 μM)

Table 1: **List and composition of microinjection solutions used for *in vivo* DAPI uptake assay.**

Thorlabs) through an objective lens (TV Lens, F1.2 8 mm, Ernitec, Ballerup, Denmark). To ensure stability and minimize light intensity fluctuation, the light source was switched on 1 h before image acquisition. To further reduce noise, the analysed image of each mouse was obtained by averaging 20 frames acquired at 0.9 frames per second.

In vivo DAPI uptake assay

Mice were anesthetized with an intraperitoneal (i.p.) injection of physiological solution containing 90 mg/kg ketamine and 0.5 mg/kg medetomidine. Half-doses of the anaesthesia were reinjected at 1.5-h intervals to avoid mouse awaking. For intradermal microinjections, the easily accessible mouse earlobe was selected after noting that dox induction promoted strong EGFP expression associated with epidermal thickening also in earlobe skin of Cx26G45E mice (Fig. S3). Injections were performed using a 10 μl syringe (NANOFIL, World Precision Instruments Inc., Sarasota, FL, USA) equipped with a 33-gauge needle. We used 4 different PBS-based microinjection solutions (Table 1).

The Ca^{2+} chelator ethylene glycol-bis(β-aminoethyl ether)-N,N,N′,N′-tetraacetic acid (EGTA, 5 mM, Cat. No. E3889, Sigma–Aldrich) was used in all solutions to promote HC opening.[51] To confirm that DAPI uptake was mediated by HCs, FFA (400 μM, Cat. No. F9005, Merck) was added to Solutions 3 and 4.[42]

After injecting 5 μl of Solution 1 or Solution 3, to estimate basal fluorescence levels, we waited 30 min. Next, we injected 5 μl of Solution 2 or Solution 4, respectively, in the same earlobe site, to measure DAPI uptake through HCs. Solution 2 and 4 contained DAPI (10 μM, Cat. No. D1306, Thermo-Fisher Scientific) and a cell-impermeant high molecular weight (MW) dextran (70,000 Da) conjugated to Texas Red (Dex.TR, 1.78 μM, Cat. No. D1830, Thermo-Fisher Scientific). Dex.TR served to visualize and delineate the tissue volume reached by the injected solution, as well as to identify cells with a compromised plasma membrane (which were penetrated by Dex.TR, and therefore excluded from the analysis).

Laser scanning intravital multiphoton microscopy in mouse earlobe skin was performed as recently described.[52] Briefly, anesthetized mice were placed on the stage of the microscope equipped with a feedback-controlled heating pad (for homeothermic control of body temperature). Mouse earlobe skin was gently cleaned with PBS, dried, and attached to the microscope stage with double-sided tape. A drop of PBS was used for optically coupling the 25 × water-immersion objective lens (XLPLN25XWMP2, NA 1.05, Olympus Corporation, Tokyo, Japan) with mouse earlobe. To determine basal skin fluorescence, $n \geq 3$ through-focus image sequences (z-stacks) were collected, with steps of 1 μm along the optical axis and with a pixel size of 619 nm. Scanning speed was 12 kHz, and each frame was averaged 20 times. Each FOV was imaged sequentially at excitation wavelengths of 780 nm and 920 nm (see below) and images were stored for off-line analysis.

After DAPI microinjection (Solution 2 or Solution 4), we waited 45 min before acquiring more z-stacks, with unchanged imaging conditions, in the Dex.TR-invaded area of earlobe skin. DAPI fluorescence, excited at 780 nm, was collected through a 460/50 nm emission filter. EGFP fluorescence, excited at 920 nm, was collected through 525/40 nm emission filter. Dex.TR. fluorescence, also excited at 920 nm, was collected through a 612/69 nm emission filter. To estimate mAb effect on DAPI uptake from keratinocytes in control animals, we also injected AAVmAb in 3 age-matched –dox mice, that were tested and analysed as described above. We pooled data from $n = 3$ mice and $m \geq 4$ FOV/mouse/condition.

Evaluation of mouse locomotion activity

To evaluate locomotion activity, each mouse was caged individually in a Digital Ventilated Cage (DVC) system[53,54] manufactured by Tecniplast SpA (Buguggiate, Italy). Data collection was based on an electronic sensing board placed underneath the cage and comprising 12 electrodes connected to an integrated circuit that sampled electrical capacitance of each electrode at 250 ms intervals. When an animal moved over one, or more electrodes, it caused a change in capacitance. If the measured change exceeded a fixed threshold, the event was counted as a valid activation of the selected electrode. The number of suprathreshold events averaged over the 12 electrodes in a selected time interval was used in scoring system to generate an "Animal Locomotion Index". For system validation and additional technical details, see.[53,54]

Histology and immunofluorescence

Skin

Mouse skin biopsies were collected from the neck region and gently flattened on a sheet of paper (Tissue-Tek II, Sakura Finetek USA, Inc., Torrance, CA, USA).

For cryosection preparation, samples were fixed in 4% paraformaldehyde (PFA) for 30 min, placed in Killik embedding medium (Cat. No. 05-9801, Bio-Optica, Milan, Italy), frozen and cut using a cryostat (CM 1850 UV, Leica Biosystems Nussloch GmbH, Nussloch, Germany). Cryo-sections (8-μm thickness) were fixed in

Antibody	Concentration	Host	Class	Cat. No.	Supplier	#RRID and reference
Anti-Cx26	1:200	Mouse	polyclonal	71–0500	Thermo-Fisher Scientific	AB_2533971 Ref. 41
Anti- Cx30	1:50	Rabbit	polyclonal	71–2200	Thermo-Fisher Scientific	AB_2533979 Ref. 55
Anti- Cx43	1:100	Rabbit	polyclonal	71–0700	Thermo-Fisher Scientific	AB_2533973 Ref. 56
Anti- E Cadherin	1:200	Rat	monoclonal	13–1900	Thermo-Fisher Scientific	AB_2533005 Ref. 57
Anti-Ki-67	1:50	Rabbit	polyclonal	PA5-19462	Thermo-Fisher Scientific	AB_10981523 Ref. 58
Anti-Cleaved Caspase-3	1:400	Rabbit	polyclonal	9661	Cell Signaling	AB_2341188 Ref. 41
Anti- Keratin1	1:500	Rabbit	polyclonal	905601	Biolegend	AB_2565051 Ref. 59
Anti-Keratin14	1:50	Mouse	monoclonal	sc-53253	Santa Cruz Biotechnology	AB_2134820 Ref. 60

Note: RRID = Research Resource Identifier (https://scicrunch.org/resources).

Table 2: **List of primary antibodies used for immunofluorescence staining.**

4% PFA for 15 min and permeabilized for 1 h at room temperature with 0.25% Tryton X-100 (Cat. No. 9002-93-1, Sigma–Aldrich) in Tris-buffered saline 1X (TBS, Cat. No. 1706435, Bio-Rad) supplemented with 5% goat serum (Cat. No. G9023, Sigma–Aldrich). Samples were incubated overnight in a humidified chamber at 4 °C with primary antibodies (Table 2) diluted in blocking buffer (5% goat serum in TBS). The next day, slides were washed 3 times with washing buffer (i.e. TBS 1X containing 0.2% Tween 20, Cat. No. P1379, Sigma–Aldrich), incubated for 1 h with cross-adsorbed fluorescent secondary antibodies (Table 3) and washed 3 times with washing buffer. Nuclei were counterstained with DAPI (5 µM, dissolved in PBS). After adding an anti-fade mounting medium (ProLong Gold, Cat. No. P36934, Thermo-Fisher Scientific), slides were coverslipped and sealed with nail polish. For immunostaining with anti-Ki-67 and anti-CC3 primary antibodies, actin filaments were stained with fluorescent phalloidin (ActinGreen, Cat. No. R37110, Thermo-Fisher Scientific).

Confocal fluorescence images were acquired with a TCS SP5 microscope (Leica) equipped with a 40 × (HCX PL Apo, UV optimized, NA 1.25) or 63 × (HC PL Apo, UV optimized, NA 1.4, Leica) oil immersion objective. DAPI fluorescence was excited by a 405-nm UV laser and collected between 415 nm and 475 nm; EGFP and actin fluorescence was excited by a 488-nm Ar laser and collected between 500 and 540 nm; red fluorescent secondary antibodies were excited by a 543-nm HeNe laser. Emission was collected between 600 nm and 660 nm (for Alexa Fluor 568 conjugated antibodies), or between 570 nm and 635 nm (for Alexa 546 and Alexa 555 conjugated antibodies). Images were acquired by averaging each line 16 times (total pixel dwell time: 0.7 ms; pixel size: 120 nm, unless otherwise stated) using a sequential line-by-line protocol.

For histology, skin samples were fixed overnight in 4% PFA at 4 °C, dehydrated in increasing alcohol concentrations and embedded in paraffin. Samples were then cut in 8-µm sections with a microtome (RM2135, Leica). Slices were deparaffinized, rehydrated and stained with hematoxylin and eosin.[61] Bright field images were acquired using an inverted microscope (LMD7000, Leica) equipped with a 40 × objective (HCX PL Fluotar, NA 0.6, Leica) and a colour camera (DFC310 FX, Leica).

Liver

Livers from age-matched –dox and –dox + AAVmAb mice, euthanized four months after caudal vein injection of the AAVmAb, were dissected, placed in Killik

Antibody	Concentration	Species reactivity	Class	Host/Isotype	Cat. No.	Supplier	#RRID
Alexa Fluor 568	1:500	Mouse	polyclonal	Goat/IgG	A-11004	Thermo-Fisher Scientific	AB_2534072
Alexa Fluor 546	1:500	Rat	polyclonal	Goat/IgG	A-11081	Thermo-Fisher Scientific	AB_2534125
Alexa Fluor 555	1:500 or 1:800	Rabbit	polyclonal	Donkey/IgG	A-31572	Thermo-Fisher Scientific	AB_162543
Alexa Fluor 488	1:300	Mouse	polyclonal	Goat/IgG	A-11029	Thermo-Fisher Scientific	AB_2534088

Table 3: **List of secondary antibodies used for immunofluorescence staining.**

embedding medium (Cat. No. 05-9801, Bio-Optica, Milan, Italy), frozen and sectioned (8 μm sections) using a cryostat (CM 1850 UV, Leica Biosystems). For immunostaining, tissue slides were fixed in ice cold acetone for 20 min at –20 °C, washed 3 times for 5 min with 1xPBS and incubated for 30 min at room temperature in blocking buffer containing 5% normal donkey serum (Cat. No. S30, Millipore) and 1% bovine serum albumin (BSA, Cat. No. A4503, Sigma–Aldrich). Samples were then incubated for 1 h at room temperature with an anti-Cx26 primary antibody (Table 2), diluted in blocking buffer, followed by washing and incubation with an Alexa Fluor 555-conjugated secondary antibody (Table 3). Nuclei were stained with DAPI (5 μM, dissolved in PBS), followed by Actin green to label actin filaments. Finally, slides were mounted with ProLong Gold.

Brain

Brains from age-matched –dox and –dox + AAVmAb mice, euthanized four months after caudal vein injection of the AAVmAb, were dissected and post-fixed overnight in 4% PFA in PBS at 4 °C. Upon embedding in 2% agar, tissues were serially sectioned (50 μm sections) using a Vibratome (VT1220s, Leica Biosystems). For immunostaining, sections were permeabilized with 0.5% Triton for 1 h at room temperature, incubated for 1 h in blocking buffer containing 5% normal donkey serum (Cat. No. S30, Millipore), 3% bovine serum albumin (BSA, Cat. No. A4503, Sigma–Aldrich) and 0.05% Tween-20 (Cat. No. 1706531, Bio-Rad Laboratories).

To evaluate gap junction formation, samples were then incubated overnight at 4 °C, with an anti-Cx30 primary antibody (Table 2) diluted in blocking buffer without BSA, followed by washing and incubation with an Alexa Fluor 555-conjugated secondary antibody (Table 3). Nuclei were stained with DAPI (5 μM, dissolved in PBS). Finally, slides were mounted with ProLong Gold.

To evaluate mAb distribution in brain areas following intracerebroventricular (ICV) injection of 5×10^{10} GC of AAVmAb in P0 mice[62] (used as positive controls), animals were euthanized four weeks after ICV injection, and brains were dissected and processed as described above. Samples were then permeabilized with 0.3% Triton for 1 h at room temperature followed by incubation with an Alexa Fluor 488-conjugated secondary antibody (Table 3) overnight at 4 °C. Nuclei were stained with DAPI (5 μM, dissolved in PBS). Finally, slides were mounted with ProLong Gold.

Antibody validation

For commercial antibodies (Tables 2 and 3) we provide relevant documentation in the Supplemental Data (Reagent Validation file). As for abEC1.1, the mAb has been a previously characterized and extensively validated both *in vitro* and *in vivo*.[31–35] Further characterization for its administration as an AAVmAb is provided in this article.

Image processing and quantification

For image processing we used the open-source software ImageJ/Fiji (ImageJ-win64) and related plugins. For data analysis and plotting we used Matlab (R2019a).

To quantify lesional skin area, the 3 colour channels (R, red; G, green; B, blue) of each acquired mouse image were separated, thus generating 3 corresponding 8-bit images, each one with pixel intensity values comprised between 0 and 255. For automated lesion identification, we calculated the pixel-by-pixel ratio of the R channel divided by the B channel (R/B intensity image). To verify uniformity and stability of image acquisition, we placed a white reflective target in a fixed position close to mouse location and verified that the mean R/B value measured within the target area did not change more than 0.5% over time. Next, we applied a 60 × 60 pxl median filter to the R/B image, thus generating a heavily low pass (lp) filtered version of it (R/B_lp) which was subtracted from the R/B image. Next, we applied an intensity threshold to the resulting high-pass (hp) filtered image (R/B_hp = R/B – R/B_lp) and we fed the result to the "*Analyze particle*" plugin to determine lesion contours. We manually discarded the contours outlining ears, paws and tail. We measured the extension of ROIs encompassed by all the remaining contours using the "*Multi Measure*" plugin.

To quantify epidermal thickness, we used the "*Wand*" plugin to select the epidermis. We then measured the local thickness of the epidermis using the "*Distance Map*" plugin, which generated a distribution of values for each image. The mean of this distribution for each image was retained as the measured parameter. The shown data are the distributions of these mean values, converted from pixel to real distances after image calibration.

To estimate Cx26 density, we applied a threshold to the red channel of immunofluorescence images. We then counted the number of suprathreshold pixels in cells that exhibited a Cx26 punctuate immunolabelling signal and evaluated Cx26 density as the number of counted pixels divided by the number of immunolabelled cells.

To quantify *in vivo* DAPI uptake, we selected 23 cell nuclei in each image and measured nuclear fluorescence as the average signal intensity within the nucleus-containing ROI using the "*Measure*" plugin. We then estimated the DAPI signal as $\Delta F = F – F_0$, where F_0 and F are the average nuclear fluorescence and the single cell nuclear fluorescence measured before and after DAPI injection, respectively.

To quantify cell size, we applied a threshold to the red channel of immunofluorescence images. We then applied a sequence of image filters ("*Smooth*", "*Erode*" and "*Dilate*") to enhance the E-cadherin signal. To extract cell border contours, we used the "*Analyze particle*" plugin. Finally, we used the "*Measure*" plugin to quantify the encompassed area.

To count the number of cells expressing a given (red fluorescent) marker, we applied a threshold to the red channel of immunofluorescence images to generate binary masks of the areas of interest. We applied the masks to the corresponding DAPI fluorescence channel and counted the number of DAPI positive cells in the masked area using the "*Analyze particle*" plugin.

To quantify CC3 expression, we calculated the number of pixels with CC3 signals as the pixels in the red fluorescence channel whose intensity exceeded a given threshold.

Statistics

Sample sizes (n) for each analysis are stated in the figure legends. The null-hypothesis of normally distributed samples was verified using the Shapiro–Wilk test. For multiple comparison, parametric analysis of variance was performed by one-way ANOVA; for pairwise comparisons, the two-tailed t-test was used. In the case of multiple comparison testing, a Bonferroni correction was applied after the ANOVA test. Non-parametric statistical analysis of variance for pairwise comparison was performed using the Mann–Whitney U test. In all statistical analysis, a p-value (P) < 0.05 indicates statistical significance. All statistical analyses were conducted using Matlab (R2019a).

Role of funders

This research was supported by Fondazione Telethon grant GGP19148 (FM), the University of Padova grant Prot. BIRD187130 (FM), the Foundation for Ichthyosis and Related Skin Types (FIRST, TWW), and the National Institutes of Health grant EY 026911 (TWW). Funders had no role in the study design, in the collection, analysis and interpretation of data, in the writing of the report and in the decision to submit the paper for publication.

Results

In vivo AAVmAb treatment reduced visible manifestations of epidermal pathology in KID syndrome

We designed a codon optimized[63] AAV transfer vector[48] expressing a single chain fragment variable-fragment crystallizable (scFv-Fc) format[47] of abEC1.1 [31–34], with a mouse Fc, under the CAG promoter.[64] We used this vector to generate virions with an AAV8 capsid,[38] and administered 1.25×10^{12} genome copies (GC) of the abEC1.1-encoding AAV8 vector to Cx26G45E mice via caudal vein injection. We refer to this procedure as *in vivo* AAVmAb treatment. We then monitored abEC1.1 (mAb) concentration in the circulation by enzyme-linked immunosorbent assay (ELISA) on serum samples[49] over a period of 70 days post-injection. Injected mice produced the encoded mAb at serum concentrations that peaked within 21 days, reaching values in excess of 50 μg/ml, and this level of expression was maintained for at least 3 more weeks (Fig. 1a). To determine which tissues were transduced by the virus, we performed caudal vein injections in a separate group of mice with an equal number of genome copies of a control AAV8 expressing the EGFP. Four weeks later, we detected high levels of EGFP expression in liver, back paw muscle and abdominal fat (Fig. S4). No significant EGFP signal was detected in other tissues, such as bone, bladder, intestine or brain.

Given that lentiviral vectors have shown some potential for gene delivery targeted to the liver in animal models,[65] and are investigated in clinical trials for gene therapy,[66] we also tested a lentivirus (LV) encoding abEC1.1 (LVmAb, see Methods section). The maximum mAb level detected after caudal vein injection of the LVmAb (Fig. S5) was more than 10-fold lower than the level achieved with the AAVmAb (Fig. 1a). Based on these results, we decided to initiate dox induction (and therefore pathology) in Cx26G45E mice 21 days after caudal vein injection of the AAVmAb. We then compared the skin pathology of dox-induced untreated (+dox) and treated (+dox + AVVmAb) mice over a 4-week period (Fig. 1b) using an *ad-hoc* developed, automated and quantitative method based on ratiometric reflectance imaging (Fig. S2, see Methods). In untreated mice, the percentage of skin area bearing KID lesions increased steadily from zero to about 27% within 4 weeks of induction, in accord with previous reports.[41,42] In contrast, skin pathology in +dox + AVVmAb mice levelled off at <7% of lesional skin area within 3 days of induction. The differences between + dox + AVVmAb mice and +dox untreated mice became significant after 14 days of induction (Fig. 1c). These results showed that expression of the AAV-encoded abEC1.1 mAb drastically improved the visible manifestations of epidermal pathology in the Cx26G45E mouse model of KID syndrome.

In vivo AAVmAb treatment reduced epidermal thickening in KID syndrome

To further characterize the effects of *in vivo* AAVmAb treatment on Cx26G45E mice, we examined histological sections of neck skin and quantified epidermal thickness (excluding the stratum corneum) from image analysis of haematoxylin and eosin (H&E) stained samples (Fig. 2a). Sections obtained from non-induced (–dox) mice showed normal thickness, whereas

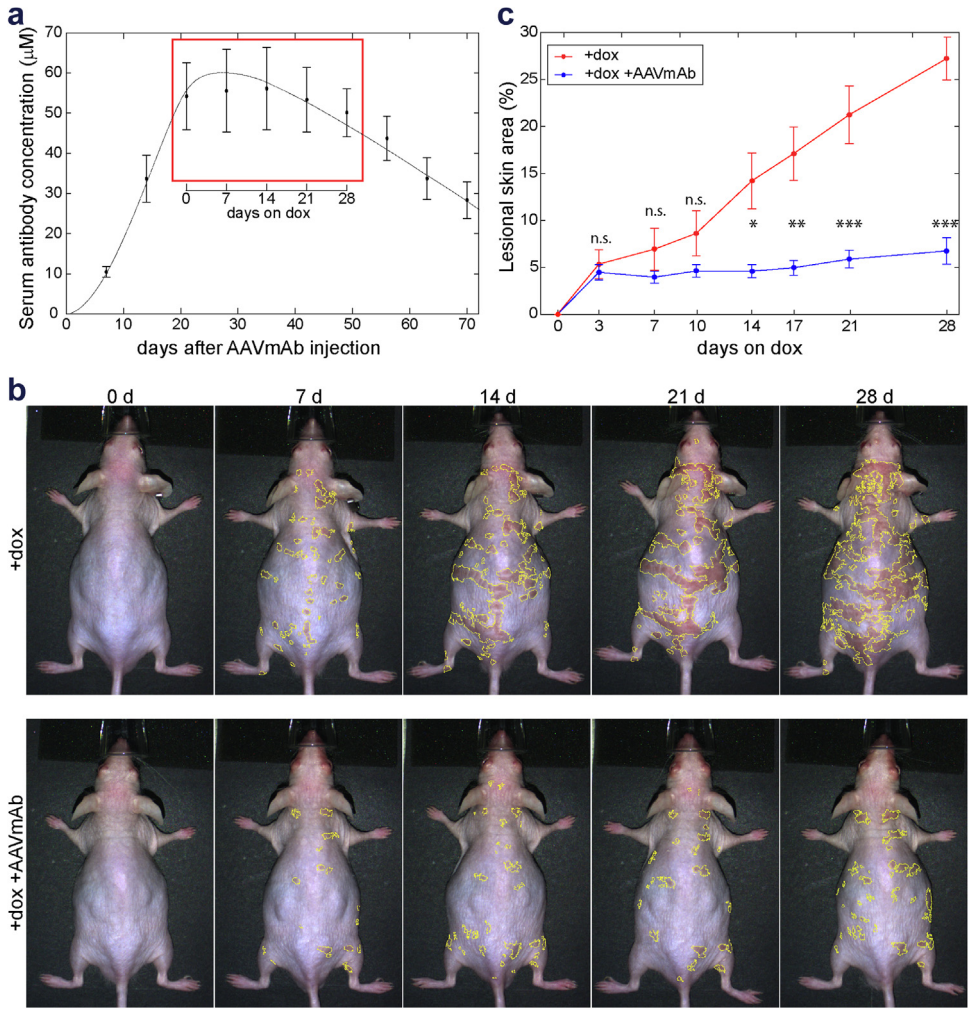

***Fig. 1:* Effect of AAVmAb treatment on epidermal pathology.** (**a**) Serum antibody concentration vs. days after AAVmAb injection, estimated by ELISA. The red inset delimits the time interval of doxycycline (dox) induction during which the cutaneous phenotype was quantified. Shown are pooled data from *n* = 6 animals. (**b**) Representative examples of epidermal lesions automatically detected by ratiometric reflectance image analysis at indicated time points after dox induction. *Top*: untreated dox-induced Cx26G45E transgenic mouse (+dox) showing typical KID pathology worsening over time. Skin lesions are shown contoured by yellow lines automatically drawn by the analysis algorithm. *Bottom*: dox-induced Cx26G45E transgenic mouse treated with AAVmAb (+dox + AAVmAb); treatment limited the growth of skin area affected by lesions. (**c**) Quantification of the lesional skin area vs. days on dox. Data are shown as mean ± standard error of the mean (s.e.m.) for untreated (*n* = 6) and treated (*n* = 6) animals; p-values (P) were computed with Mann–Whitney U statistical test. *, P < 0.05; **, P < 0.01; ***, P < 0.005; P > 0.05 was considered not significant (n.s.).

Cx26G45E mice induced for 28 days (+dox) had a 3.5-fold increase in mean epidermal thickness. In + dox antibody treated mice (+dox + AAVmAb), the mean epidermal thickness was significantly reduced compared to untreated + dox littermates, and not significantly different from that of –dox littermates (not induced with dox and injected with vehicle, Fig. 2b). These data showed that expression of the AAV-encoded abEC1.1 mAb had a beneficial effect, reducing the epidermal thickening promoted by dox induction in the Cx26G4E mouse model of KID syndrome.

In vivo AAVmAb treatment did not interfere with Cx26 expression in lesional epidermis

Maintenance of a normal and healthy epidermal barrier relies on a delicate balance between proliferation and differentiation of epidermal stem cells,[67,68] two cellular processes that are critically influenced by Cx expression.[2,4] In prior work, skin disease development in Cx26G45E mice correlated with mutant connexin expression induced by dox.[42] Here, we confirmed by immunofluorescence analysis of neck skin cryosections that Cx26 was expressed at undetectable levels in –dox

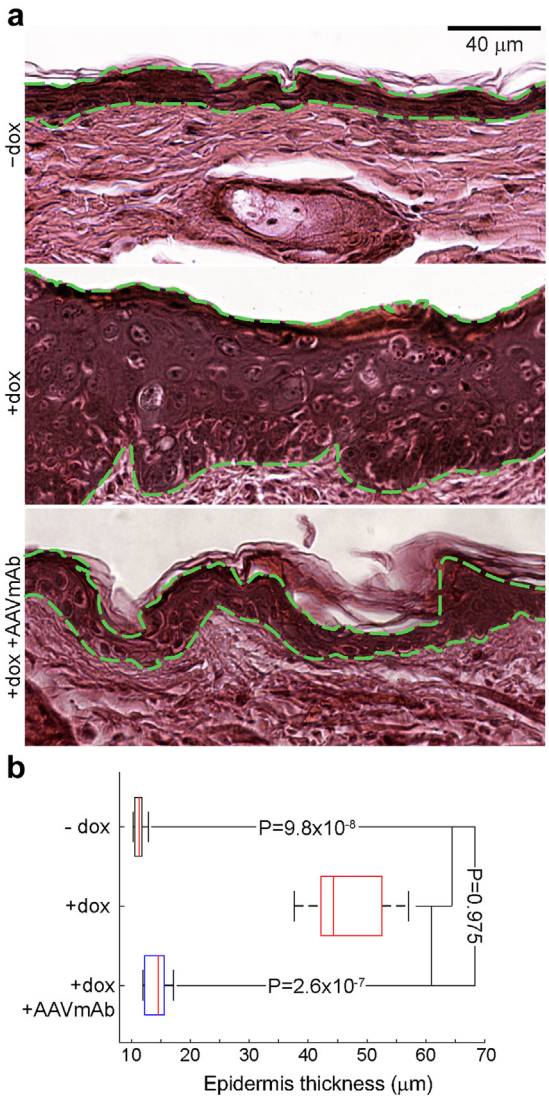

Fig. 2: **Transverse sections of neck skin from treated and untreated animals stained with haematoxylin and eosin (H&E).** (**a**) Representative microphotographs from Cx26G45E transgenic mice not induced with dox (–dox, *n* = 5), induced with dox for 28 days (+dox, *n* = 6), induced with dox for 28 days and treated with AAVmAb (+dox + AAVmAb, *n* = 5). Epidermal layers are shown encompassed between dashed green lines. Scale bar, 40 µm; objective: 40 × . (**b**) Box plots showing distributions of epidermis thickness estimated from H&E image analysis; shown are pooled data from the given number of mice and $m \geq 3$ fields of view (FOVs)/mouse/condition. The midline in each box represents the median whereas whiskers correspond to the first and third quartile. P denotes p-values, computed with ANOVA statistical test.

Cx26G45E mouse epidermis. Following dox induction, the commercial anti-Cx26 selective antibody used for these experiments (which did not distinguish between the wild type and the p.G45E variant of the protein) revealed a well-defined punctuate pattern of Cx26 expression throughout the EGFP-expressing thickened epidermis (Fig. 3a). In + dox + AAVmAb mice, Cx26 immunolabeling persisted with unchanged density in the epidermis (Fig. 3b), whose thickness was significantly reduced by AAVmAb treatment (Fig. 2). Therefore, *in vivo* AAVmAb treatment did not reduce Cx26 expression in lesional epidermis, presumably achieving improvement of pathology through blocking the activity of mutant HCs.

In vivo AAVmAb treatment reduced dye uptake through epidermal HCs

In prior work we showed increased HC currents in transgenic keratinocytes obtained from Cx26G45E mice.[41] Furthermore, by overexpressing the p.G45E pathological variant of Cx26 in HaCaT cells (a spontaneously immortalized line of aneuploid human keratinocytes[69]) we previously showed that the purified abEC1.1 mAb inhibited mutant leaky HCs, as assessed by measurement of whole cell currents[31] and ionized calcium (Ca^{2+}) uptake.[33] Here, we used 4′,6-diamidino-2-phenylindole (DAPI) to determine whether *in vivo* AAVmAb treatment reduced HC function in keratinocytes. For these *in vivo* dye uptake experiments, we exploited the property that DAPI permeates though open HCs and is non fluorescent unless bound to nucleic acids.[70] Following DAPI intradermal microinjection in the earlobe skin (see Methods), we performed intravital multiphoton fluorescence microscopy[52] and detected low levels of DAPI uptake in both –dox mice and –dox + AAVmAb mice (Fig. 4a). This background DAPI uptake was likely due to Cx43 HCs, given that (i) Cx43 is the prevalent isotype expressed in mouse interfollicular epidermis[52] and (ii) Cx43 HCs are insensitive to abEC1.1.[32] Pathology induction with dox (+dox) resulted in a 6.8-fold increase of the mean DAPI uptake (Fig. 4b), consistent with overexpression of Cx26 (Fig. 3). DAPI uptake was reduced 2.6-fold in +dox + AAVmAb mice (Fig. 4b). DAPI uptake was also reduced 12-fold by co-microinjection of flufenamic acid (FFA, 400 µM), a well-known and widely used non-specific blocker of HCs,[42] in +dox mice (+dox + FFA, Fig. 4b). Together, data in Figs. 3 and 4 suggest that (i) improvement in skin pathology imparted by *in vivo* AAVmAb treatment was not due to off-target interference with the transgenic expression of the mutated connexin and (ii) the abEC1.1 therapeutic mechanism of action entails blockade of HCs, in accord with prior *in vitro*[31–33] and *in vivo* work.[34]

The fact that DAPI was uptaken equally in –dox and –dox + AAVmAb mice (Fig. 4), supports the tenet that *in vivo* AAVmAb treatment did not modify the baseline expression level of epidermal HCs. On the other hand, FFA microinjection in earlobe skin (+dox + FFA condition in Fig. 4), which aspecifically blocks several

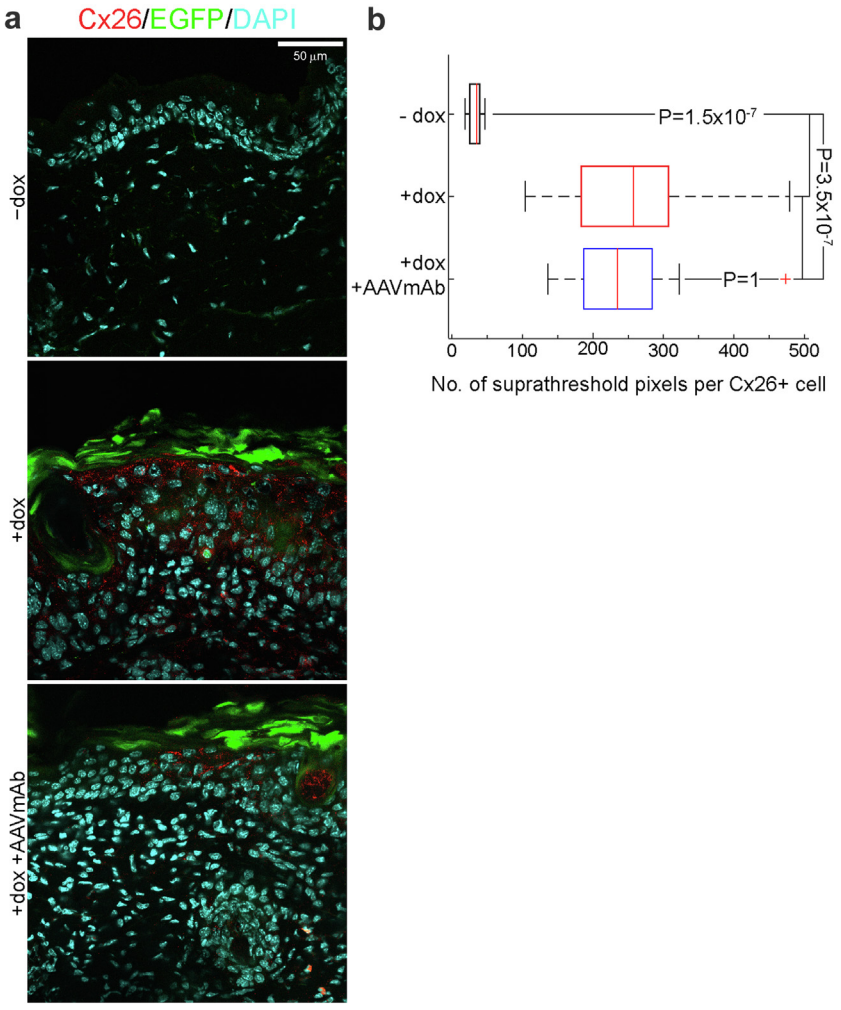

Fig. 3: **Effect of AAVmAb treatment on Cx26 expression in the epidermis.** (**a**) Representative confocal immunofluorescence images of neck skin transverse sections from –dox, +dox and +dox + AAVmAb mice. Samples were labelled with a selective anti-Cx26 antibody (red) directed against the protein C-terminus. As such, the antibody did not discriminate between wild type and mutant Cx26. Nuclei were counterstained with DAPI (cyan). The green signal in the thickened epidermis of +dox animals is due to EGFP expression downstream of the Cx26G45E coding sequence. Note the punctate pattern of Cx26 staining in +dox mice, which was undetectable in –dox mice and reduced in +dox + AAVmAb animals. Scale bar, 50 µm; objective: 63 × . (**b**) Box plots showing distributions of Cx26 density in cells labelled by the commercial anti-Cx26 antibody for each condition. Shown are pooled data from n = 3 mice and m = 4 FOV/mouse/condition. The red cross represents an outlier. P denotes p-values computed with ANOVA statistical test.

different types of HCs, reduced DAPI uptake more than *in vivo* treatment with the AAVmAb, suggesting that HC isoforms not targeted by abEC1.1 (most likely, Cx43) were upregulated by dox induction. To test this hypothesis, we performed immunofluorescence analysis of skin samples and found that dox exposure increased the expression not only of Cx26 (Fig. 3) but also of Cx43 (whose HCs are not blocked by abEC1.1) and Cx30 (whose HCs are blocked by abEC1.1) (Fig. S6). Therefore, Cx43 HCs could account for the different blocking efficacy of *in vivo* AAVmAb treatment vs. FFA microinjection in the earlobe skin of +dox animals.

In vivo AAVmAb treatment significantly reduced keratinocyte size and number

To better characterize the effects of AAVmAb treatment at the cellular and molecular level, we performed immunofluorescence studies with selected markers, as detailed hereafter. In human KID patients carrying the p.G45E mutation of Cx26, it has been shown that keratinocyte size was increased within lesional skin biopsies.[30] Similarly, it was previously reported that keratinocytes from +dox Cx26G45E mice were significantly larger than those from –dox littermate controls, and that cell size increased with disease progression.[41]

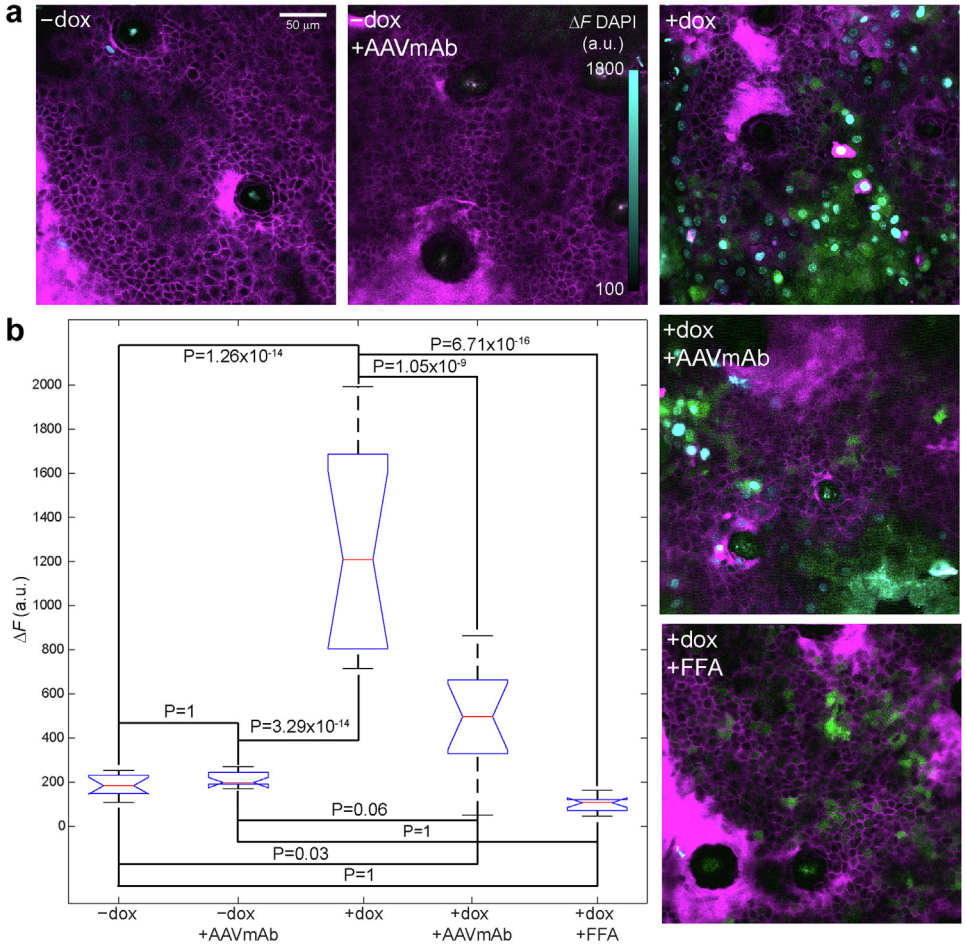

***Fig. 4: In vivo* DAPI uptake.** (**a**) Representative fluorescence images of earlobe skin from –dox, +dox, +dox + AAVmAb and –dox + AAVmAb mice. Images were acquired 45 min after intradermal injection of Ca^{2+}-free PBS supplemented with EGTA (5 mM), DAPI (10 µM, cyan) and Dextran Texas Red (1.79 µM, magenta); +FFA denotes addition of FFA (400 µM) to the injection solution. The green signal in +dox images is due to EGFP expression downstream of the Cx26G45E coding sequence. Scale bar, 50 µm; objective: 25 × . (**b**) Box plots showing distributions of DAPI fluorescence (*F*) intensity change ($\Delta F = F–F_0$), where F_0 is background fluorescence level, measured before intradermal injection of DAPI. Shown are pooled data from $n = 3$ mice and $m = 4$ FOV/mouse/condition. P denotes p-values computed with ANOVA statistical test.

Therefore, after 28 days of dox induction, we quantified keratinocyte size and number in skin cryosections immunolabelled with an anti-E-cadherin antibody that clearly delineates cell contours in the epidermis (Fig. 5a). In + dox mice, keratinocyte cross sectional area increased significantly, by 1.5-fold, compared to –dox mice and was reduced to pre-dox levels in +dox + AAVmAb mice (Fig. 5b). In addition, the number of keratinocytes in fixed-size microscope field of views (FOVs) comprising the epidermis increased significantly, by 3.0-fold, and was reduced to pre-dox levels by AAVmAb treatment (Fig. 5c), in good agreement with the results of Figs. 2 and 3. These results suggest that the epidermis was returning to a non-disease state, characterized by normal sized keratinocytes, following expression of the AAV-encoded abEC1.1 mAb.

In vivo AAVmAb treatment restored expression levels of proliferation and apoptosis markers

It was previously reported that both cell division and cell death were modulated in the diseased skin of Cx26-G45E animals, with elevated staining for phospho-histone-3 observed in the epidermis, and increased expression of cleaved caspase-3 (CC3) in the dermis.[41] To confirm that epidermal thickening correlated with abnormal keratinocyte proliferation, we examined the expression of Ki-67 protein, a widely used proliferation marker[71] (Fig. 6a). Dox induction increased the mean level of Ki-67 expression by 3.5-fold, and *in vivo* AAVmAb treatment recovered a normal Ki-67 level (Fig. 6b). We further confirmed that apoptosis was elevated in the dermis and that dox induction increased the mean level of CC3 by 23-fold (Fig. 7a). Once again, AAVmAb treatment reduced CC3 expression by 10.5-fold

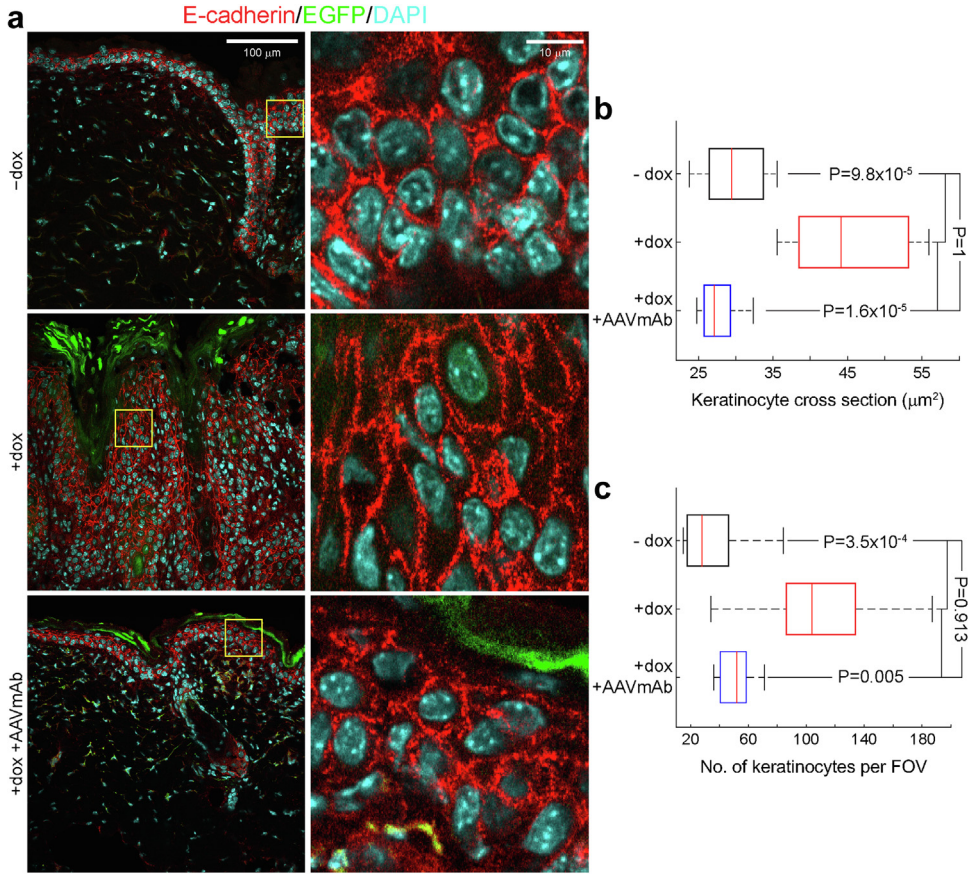

Fig. 5: **Effect of AAVmAb treatment on size and number of epidermal keratinocytes**. (**a**) Representative confocal immunofluorescence images of neck skin transverse sections from –dox, +dox and +dox + AAVmAb mice (see caption of Fig. 2). The green signal in the thickened epidermis of +dox animals is due to EGFP expression downstream of the Cx26G45E coding sequence.[41] Samples were labelled with a selective anti-E-cadherin antibody (red), and nuclei were counterstained with DAPI (cyan). Images in the right columns (scale bar, 10 µm) are magnified views of the areas contoured by squared yellow ROIs in the corresponding images at left (scale bar, 100 µm); objective: 40 × . (**b**, **c**) Box plots showing distributions of keratinocyte cross sections, estimated as the area encompassed by the E-cadherin labelled cell contours (b) and number of keratinocytes per field of view (FOV, c). Shown are pooled data from n = 3 mice and $m \geq 4$ FOV/mouse/condition. P denotes p-values computed with ANOVA statistical test.

compared to the +dox untreated animals (Fig. 7b). These data confirm restoration of the normal epithelial proliferation, and cessation of elevated apoptosis after expression of the AAV-encoded abEC1.1 mAb.

In vivo AAVmAb treatment recovered expression pattern of epidermal keratins

Keratins (Ks), the major components of the epithelial cytoskeleton, are well known diagnostic markers important for maintaining keratinocyte integrity and structural stability.[72] Type I and type II Ks form heterodimers and characteristic heterodimer patterns are found within a given epidermal cell layer, according to the degree of differentiation. Thus, K14 and K5 constitute the prevalent type I-type II heterodimer expressed in proliferative basal keratinocytes of interfollicular epidermis. In contrast, differentiated keratinocytes of the suprabasal layers express K10-K1 as the major heterodimer, and downregulate the K14-K5 pair.[73] Expression levels, cellular localization or posttranslational modifications of Ks are altered by injury and/or disease.[72]

To analyse changes in the epidermis structure due to pathology induction, we quantified K1 and K14 expression as a measure of keratinocytes organization in suprabasal and basal epidermal layer, respectively, using selective anti-Ks antibodies to immunolabel neck skin cryosections from Cx26G45E mice. We thus determined that dox induction caused complete disarray of K1 and K14 expression, with both markers expressed throughout the thickened epidermis of +dox Cx26G45E mice. *In vivo* AAVmAb treatment recovered the normal expression pattern of both markers (Fig. 8a). The mean number of cells expressing K1 increased 3.3-fold after

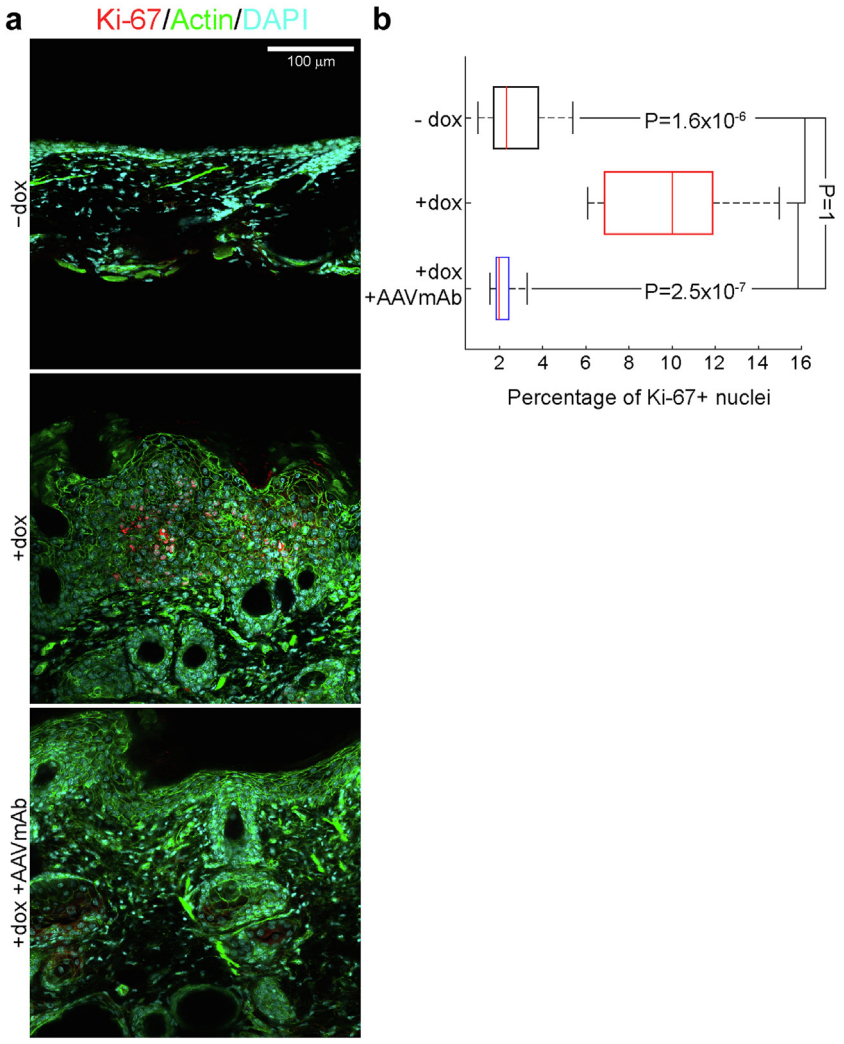

Fig. 6: **Effect of AAVmAb treatment on expression of proliferation (Ki-67) marker in the epidermis.** (**a**) Representative confocal immunofluorescence images of neck skin transverse sections from –dox, +dox and +dox + AAVmAb mice. Samples were labelled with a selective anti-Ki-67 antibody (red), nuclei were counterstained with DAPI (cyan) and actin filaments were labelled by fluorescent phalloidin (green). Scale bar, 100 µm; objective: 40 × . (**b**) Box plots showing distributions of percentage of Ki-67 positive (+) nuclei. Shown are pooled data from *n* = 3 mice and *m* = 4 FOV/mouse/condition. P denotes p-values computed with ANOVA statistical test.

dox induction and was reduced 2.6-fold by AAVmAb treatment (Fig. 8b). Likewise, the mean number of cells expressing K14 increased 4.1-fold after dox induction and was reduced 4.7-fold by AAVmAb treatment (Fig. 8c). Together, data in Figs. 5–8, showed that expression of the AAV-encoded abEC1.1 mAb had a beneficial effect on selected molecular markers of skin homeostasis and structure.

In vivo AAVmAb treatment had no adverse effects

In theory, an antibody might interact with committed HCs preventing the formation of intercellular gap junction channels, and this may potentially cause unwanted side effects.[74] Given that the liver had the highest level of viral transduction following caudal vein injection of the EGFP-encoding AAV8 control vector (Fig. S4), we examined gap junctions in liver of treated and untread mice. Quantitative image analysis of liver cryosections immunolabelled with a commercial anti-Cx26 selective antibody showed *in vivo* AAVmAb treatment affected neither the individual size nor the overall number of Cx26 gap junctions in –dox + AAVmAb mice compared to age-matched untreated controls (–dox, Fig. S7).

There is strong evidence that naturally occurring AAV serotypes have severely limited transduction efficiency in the brain owing to the stringency of the blood–brain barrier.[75] Consistent with this tenet, our

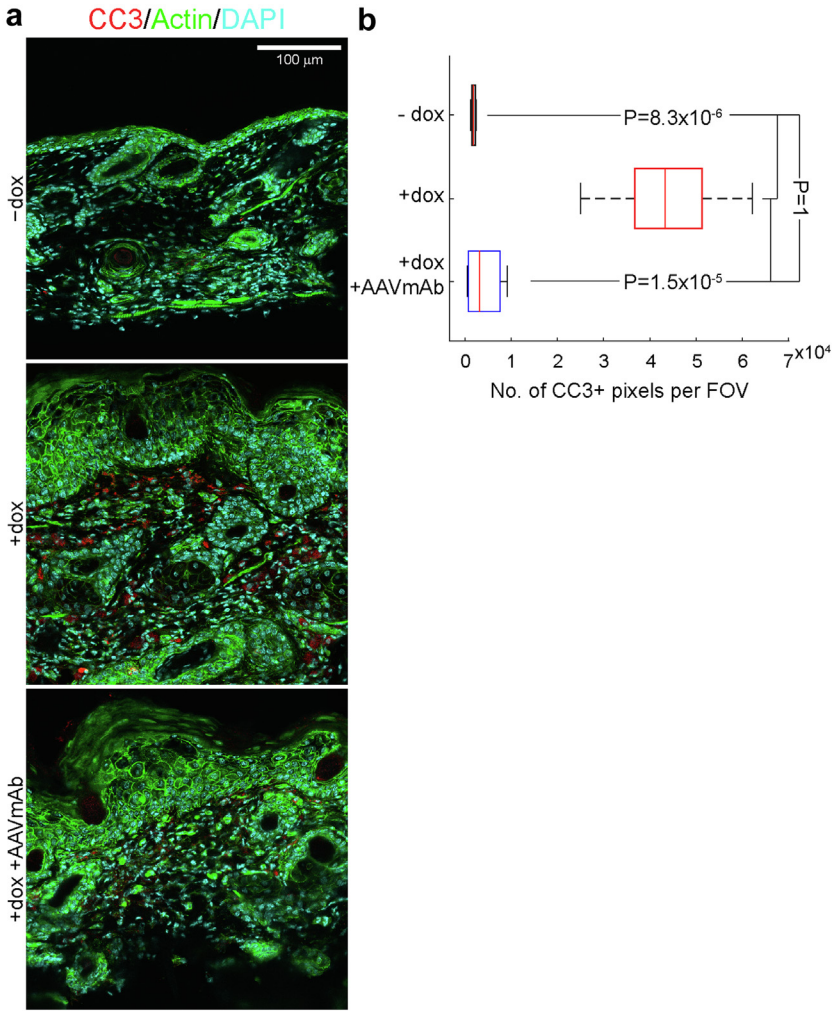

***Fig. 7*: Effect of AAVmAb treatment on expression of apoptosis marker Cleaved-Caspase3 (CC3) in the epidermis**. (**a**) Representative confocal immunofluorescence images of neck skin transverse sections from –dox, +dox and +dox + AAVmAb mice. Samples were labelled with a selective anti-CC3 antibody (red), nuclei were counterstained with DAPI (cyan) and actin filaments were labelled by fluorescent phalloidin (green). Scale bar, 100 µm; objective: 40 × . (**b**) Box plots showing distributions of No. of suprathreshold CC3+ pixels. Shown are pooled data from *n* = 3 mice and *m* = 4 FOV/mouse/condition. P denotes p-values computed with ANOVA statistical test.

immunofluorescence analysis of brain sections failed to detect abEC1.1 expression in the brain of mice subjected to *in vivo* AAVmAb treatment (Fig. S8a). To further exclude that *in vivo* AAVmAb treatment interfered with gap junction formation in the brain, we analysed a major abEC1.1 target, Cx30,[34] with widespread brain expression.[76] In different areas of brain slices immunolabelled with a commercial anti-Cx30 selective antibody, there was no difference between treated (–dox + AAVmAb) mice and age-matched controls (–dox, Fig. S8b). Likewise, body weight, food, and water consumption (Figs. S9 and S10), as well as locomotion activity (Figs. S11 and S12) were statistically indistinguishable in treated and untreated animals.

Discussion

Current treatments for KID syndrome are largely palliative and include antibiotics, surgical debridement, keratolytics, and retinoids.[77,78] The recent development of specific antibody blocking agents that target Cx HCs[31–33] allows treatment paradigms to move from palliative to therapeutic.[35] In prior work with a related mouse model of Cx-related genodermatosis (Clouston syndrome),[79,80] we demonstrated the *in vivo* efficacy of the purified abEC1.1 mAb delivered systemically, via intraperitoneal (i.p.) injection, or topically, in a cream formulation.[34] In the current study, we have attempted to use antibody gene transfer[38–40] to treat the epidermal features of KID syndrome in a mouse model that replicates the human disease.[41,42]

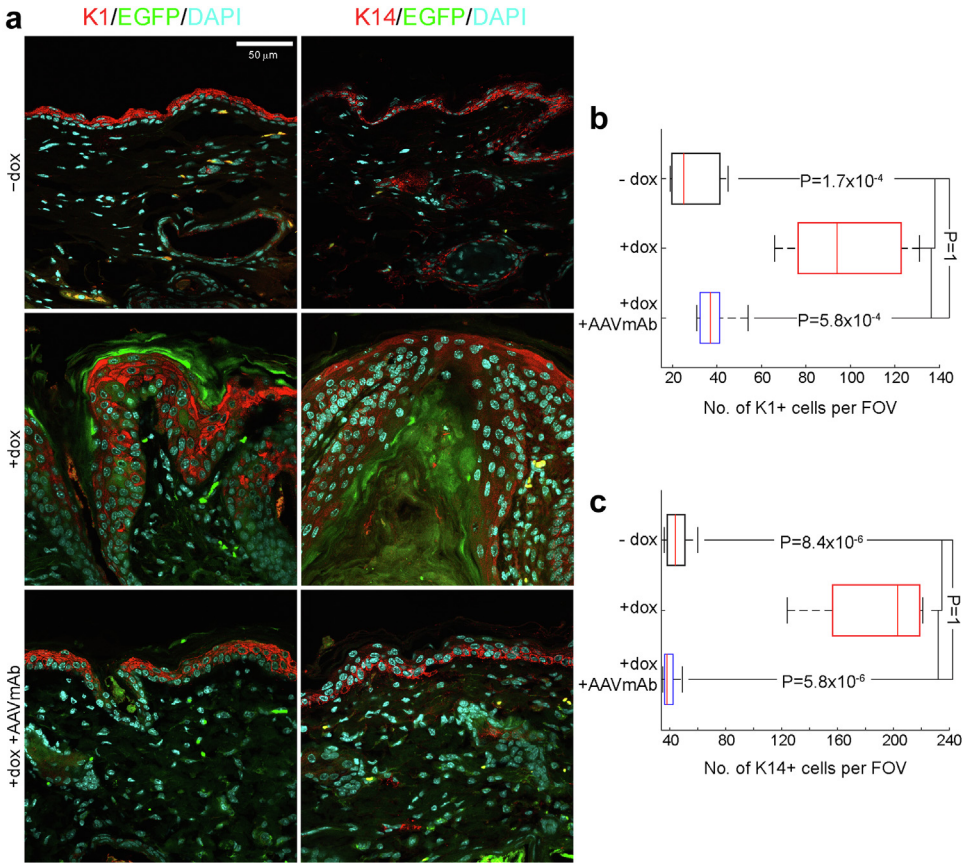

Fig. 8: **Effect of AAVmAb treatment on cytokeratin 1 (K1) and cytokeratin 14 (K14) distribution in the epidermis.** (**a**) Representative confocal immunofluorescence images of neck skin transverse sections from –dox, +dox and +dox + AAVmAb mice. Samples were labelled with selective anti-K1 (*left*) and anti-K14 (*right*) antibodies (red) and nuclei were counterstained with DAPI (cyan). The green signal in the thickened epidermis of +dox animals is due to EGFP expression downstream of the Cx26G45E coding sequence. Scale bar, 50 µm; objective: 63 × . (**b**, **c**) Box plots showing distributions of number (No.) of K1 positive (+) cells (b) and No. of K14+ cells (c). Shown are pooled data from n = 3 mice and m = 4 FOV/mouse/condition. P denotes p-values computed with ANOVA statistical test.

Our results show that AAVmAb treatment significantly reduced the size and thickness of KID lesions, and blocked dye uptake through mutant HCs in the epidermis *in vivo*. In addition, AAVmAb treatment restored normal keratinocyte proliferation and cell size, reduced apoptosis, and re-established normal patterns of keratin expression. These findings provide further support for the view that increased HC activity is a significant driver of skin pathology in KID syndrome.[9–22] They also highlight the potential of anti-HC antibodies and genetic based delivery systems for new therapeutic interventions aimed at treating the mechanistic basis of this disease.

The AAV vector approach can be used to maintain therapeutic levels of mAb over extended periods of time.[81] In fact, AAV vectors are widely recognized for their ability to direct long term stable expression of both intracellular and secreted proteins. Factors that can impact sustained vector expression include serotype of the vector, the promoter utilized to direct expression, and route of delivery.[81] Using AAV8 vectors encoding a vector that encoded both a heavy and light antibody chains for anti VEGFR2 under the control of the CAG promoter, sustained expression around 600µg/ml was demonstrated for at least 4 months following hepatic portal vein delivery.[38] More recent studies report expression for the life of the mouse using a tandem liver-muscle promoter.[82] Although in our study the level of expression showed some decline, it is possible the steady state levels is sufficient for a corrective phenotype. In addition, further vector optimization could improve our results.[83]

To further support the clinical potential of our approach, we showed that prolonged exposure to mAb had no effect on gap junction formation in liver and brain. In addition, there are two major factors that argue that interference with Cx26 gap junctions by the antibody may not occur or may not be pathologically

relevant. First, the antibody is directed to an epitope in the extracellular loop of Cx26, which is exposed in the HC configuration, but bound to the opposing HC in the gap junction channel configuration. Related to this, there would be significant steric hindrance to getting the antibody into the extracellular space in an intact gap junction, which is very small, and often adjacent to the tight junction barrier. Second, the most common non-syndromic deafness causing mutation in the GJB2 gene (delg35) causes a premature truncation of the Cx26 protein in the amino terminus. Many thousands of living humans worldwide are homozygous carriers of this allele and have no functional Cx26 channels of any type. The patients have no-known liver or brain pathologies, and only suffer hearing loss, suggesting that total loss of Cx26 activity is not generally detrimental to human health. We also provided evidence that prolonged expression of mAb did not affect body weight, food or water consumption of treated mice up to 4 months after AAVmAb injection. However, also the effect of prolonged use of an antibody directed against extracellular loops on gap junction functionality has to be investigated. This requires functional dye transfer experiments in different organs that need to be performed before any clinical application.

mAb therapy has changed the landscape of modern medicine as mAbs have emerged as a major class of therapeutic agents on the market, and have stimulated intense and widespread interest in developing treatments for diverse human disorders.[84] Several factors contribute to the success of mAbs as therapeutics, including high specificity, low toxicity and slow clearance rates,[84] in addition to the rapidly advancing gene therapy space,[48] the potency of viral vectors to mediate expression of mAbs[39] as well as promising data from long-lasting therapeutic levels of antibodies.[40]

Critical steps that need to be taken for these and related results[34] to be applied in the clinic comprise industry-standard mAb manufacturing and testing, aiming to produce purified mAb material. This can be done by generating suitable DNA constructs followed by stable CHO cell pool generation to express the desired antibodies.[85] Cell pools will have to go through a cloning procedure and clones will be assessed regarding growth, phenotype, and productivity. From top performing clones, research cell banks (RCBs) can be generated and undergo a stability study to assure productivity over time. Lead clones will undergo upstream and downstream production processes, including 10-L fed-batch, harvest and two step purification (protein A and ion-exchange chromatography). Final products will be stored in PBS to accommodate the needs for subsequent studies.[86] To ensure the quality, safety, and efficacy of biopharmaceutical products, it is necessary to perform mAb testing for stability, toxicity, immunogenicity, pharmacokinetics, pharmacodynamics and biodistribution *in vivo* assays, including all preclinical safety evaluation studies deemed necessary after careful regulatory assessment,[87] in line with good laboratory practice (GLP) and ICH S6(R1) directives.

A limitation of this study is that the pathogenetic mechanism whereby HC opening leads to disruption of epidermal homeostasis remains partially unaddressed. The opening of HCs promotes the influx of ionized calcium (Ca^{2+})[88–92] as well as diffusive release of paracrine messengers, including ATP.[51,93–97] Therefore, our working hypothesis is that, by binding to purinoceptors expressed in keratinocytes,[98] extracellular ATP released though HCs not only may trigger inflammation,[99] which can lead to further HC opening and promote cell death,[100–102] but may also upset the delicate Ca^{2+}-dependent proliferation/differentiation balance in the epidermis,[103,104] leading to breakdown of epidermal integrity.[105] This hypothesis is amenable to direct testing by generating and using improved mouse models of disease. For example, replacing the EGFP expressed in Cx26G45E mice after dox induction with a genetically encoded indicator of cytosolic Ca^{2+}[106] would allow the study of Ca^{2+} signalling directly, by intravital multiphoton microscopy of mouse skin.[52] To unravel the interplay between cytosolic Ca^{2+} and ATP release *in vivo*, an even more sophisticated animal model could be made to express also a spectrally separated indicator for ATP[107] anchored to the extracellular leaflet of the keratinocyte plasma membrane.

Dysregulated HCs are likely to play a pathogenic role in several other connexin skin disorders.[2,17,80,108,109] The results presented here, and in previous studies,[34,42] suggest that targeting this acquired activity could have tremendous benefits in the development of novel therapies for these genodermatoses. Since HC dysfunction has been implicated as a pathological mechanism in several connexinopathies beyond the skin, our findings could also lead to new therapeutic approaches to treating connexin disorders manifesting in a wide variety of organs (summarized in Table 3 of Ref.[35]).

Contributors

Conceptualization: CS, TWW, FM.
Methodology: CP, CS, AV, AC, FS, MR, FZ, GY, TWW, FM.
Investigation: CP, CN, SP, TO, DM, CDP, MR.
Visualization: CP, FM.
Funding acquisition: TWW, FM.
Project administration: FM.
Supervision: FM.
Writing – original draft: CP, FM.
Writing – review & editing: CP, CS, TWW, FM.
CP, TWW, FM had directly accessed and verified the underlying data.
All authors have read and approved the final version of the manuscript.
All authors had final responsibility for the decision to submit the paper.

Data and materials availability

Data were archived in a repository handled by the University of Padova and can be accessed at: https://researchdata.cab.unipd.it/817/.

ImageJ/Fiji scripts used for image quantification in this article are available on the GitHub repository at https://github.com/chiaraperes/AAVmAb_effect.

Declaration of interests

Drs. G. Yang, F. Zonta and F. Mammano report a patent family: "WO2017128880 – Fully human antibody specifically inhibiting connexin 26", Inventors: Qu Z, Yang G, Mammano F, Zonta F, International application number: PCT/CN2016/109847, granted to ShanghaiTech University; and a patent family "WO2020237491 – Composition and Methods to treat Ectodermal Dysplasia 2, Clouston Type", Inventors: Mammano F, Yang G, Zonta F, International Application No.: PCT/CN2019/088689, pending to ShanghaiTech University. M. Rigamonti is an employee of Tecniplast SpA. Tecniplast SpA did not have any role in the study design, decision to publish, or preparation of the manuscript. All other authors declare that they have no competing interests.

Acknowledgments

We thank Luigi Naldini (Università Vita e Salute San Raffaele, Milan, Italy) for the gift of HIV-derived lentiviral backbone vector, packaging plasmids pMDL, pVSV-G, and pRSV-Rev, Emerald Perlas (EMBL-Rome) for help with immunofluorescence and histological protocols, Giorgio Rosati (Techniplast) for assistance with the DVC system for automatic locomotion detection, Daniele Iannilli and Massimiliano Iannilli for technical assistance with ELISA procedure, Fabrizio Bonaventura for mouse blood sample collections and intravenous injections, and EMMA staff for mouse colony management and genotyping.

Appendix A. Supplementary data

Supplementary data related to this article can be found at https://doi.org/10.1016/j.ebiom.2023.104453.

References

1 Morren MA, Legius E, Giuliano F, Hadj-Rabia S, Hohl D, Bodemer C. Challenges in treating genodermatoses: new therapies at the horizon. *Front Pharmacol*. 2021;12:746664.
2 Lilly E, Sellitto C, Milstone LM, White TW. Connexin channels in congenital skin disorders. *Semin Cell Dev Biol*. 2016;50:4–12.
3 Laird DW, Lampe PD. Therapeutic strategies targeting connexins. *Nat Rev Drug Discov*. 2018;17(12):905–921.
4 Laird DW, Lampe PD. Cellular mechanisms of connexin-based inherited diseases. *Trends Cell Biol*. 2022;32(1):58–69.
5 Retamal MA, Reyes EP, Garcia IE, Pinto B, Martinez AD, Gonzalez C. Diseases associated with leaky hemichannels. *Front Cell Neurosci*. 2015;9:267.
6 Retamal MA, Fernandez-Olivares A, Stehberg J. Over-activated hemichannels: a possible therapeutic target for human diseases. *Biochim Biophys Mol Basis Dis*. 2021;1867(11):166232.
7 Wang N, De Bock M, Decrock E, et al. Paracrine signaling through plasma membrane hemichannels. *Biochim Biophys Acta*. 2013;1828(1):35–50.
8 Saez JC, Leybaert L. Hunting for connexin hemichannels. *FEBS Lett*. 2014;588(8):1205–1211.
9 Gerido DA, DeRosa AM, Richard G, White TW. Aberrant hemichannel properties of Cx26 mutations causing skin disease and deafness. *Am J Physiol Cell Physiol*. 2007;293(1):C337–C345.
10 Lee JR, Derosa AM, White TW. Connexin mutations causing skin disease and deafness increase hemichannel activity and cell death when expressed in Xenopus oocytes. *J Invest Dermatol*. 2009;129(4):870–878.
11 Sanchez HA, Mese G, Srinivas M, White TW, Verselis VK. Differentially altered Ca2+ regulation and Ca2+ permeability in Cx26 hemichannels formed by the A40V and G45E mutations that cause keratitis ichthyosis deafness syndrome. *J Gen Physiol*. 2010;136(1):47–62.
12 Levit NA, Mese G, Basaly MG, White TW. Pathological hemichannels associated with human Cx26 mutations causing Keratitis-Ichthyosis-Deafness syndrome. *Biochim Biophys Acta*. 2012;1818(8):2014–2019.
13 Lopez W, Gonzalez J, Liu Y, Harris AL, Contreras JE. Insights on the mechanisms of Ca(2+) regulation of connexin26 hemichannels revealed by human pathogenic mutations (D50N/Y). *J Gen Physiol*. 2013;142(1):23–35.
14 Mhaske PV, Levit NA, Li L, et al. The human Cx26-D50A and Cx26-A88V mutations causing keratitis-ichthyosis-deafness syndrome display increased hemichannel activity. *Am J Physiol Cell Physiol*. 2013;304(12):C1150–C1158.
15 Sanchez HA, Villone K, Srinivas M, Verselis VK. The D50N mutation and syndromic deafness: altered Cx26 hemichannel properties caused by effects on the pore and intersubunit interactions. *J Gen Physiol*. 2013;142(1):3–22.
16 Sanchez HA, Bienkowski R, Slavi N, Srinivas M, Verselis VK. Altered inhibition of Cx26 hemichannels by pH and Zn2+ in the A40V mutation associated with keratitis-ichthyosis-deafness syndrome. *J Biol Chem*. 2014;289(31):21519–21532.
17 Shuja Z, Li L, Gupta S, Mese G, White TW. Connexin26 mutations causing palmoplantar keratoderma and deafness interact with Connexin43, modifying gap junction and hemichannel properties. *J Invest Dermatol*. 2016;136(1):225–235.
18 Sanchez HA, Slavi N, Srinivas M, Verselis VK. Syndromic deafness mutations at Asn 14 differentially alter the open stability of Cx26 hemichannels. *J Gen Physiol*. 2016;148(1):25–42.
19 Taki T, Takeichi T, Sugiura K, Akiyama M. Roles of aberrant hemichannel activities due to mutant connexin26 in the pathogenesis of KID syndrome. *Sci Rep*. 2018;8(1):12824.
20 Richard G, Rouan F, Willoughby CE, et al. Missense mutations in GJB2 encoding connexin-26 cause the ectodermal dysplasia keratitis-ichthyosis-deafness syndrome. *Am J Hum Genet*. 2002;70(5):1341–1348.
21 van Steensel MA, van Geel M, Nahuys M, Smitt JH, Steijlen PM. A novel connexin 26 mutation in a patient diagnosed with keratitis-ichthyosis-deafness syndrome. *J Invest Dermatol*. 2002;118(4):724–727.
22 Garcia IE, Bosen F, Mujica P, et al. From hyperactive Connexin26 hemichannels to impairments in epidermal calcium gradient and permeability barrier in the keratitis-ichthyosis-deafness syndrome. *J Invest Dermatol*. 2016;136(3):574–583.
23 Sybert VP. *Genetic Skin Disorders*. Oxford University Press; 2017.
24 Coggshall K, Farsani T, Ruben B, et al. Keratitis, ichthyosis, and deafness syndrome: a review of infectious and neoplastic complications. *J Am Acad Dermatol*. 2013;69(1):127–134.
25 Lilly E, Bunick CG, Maley AM, et al. More than keratitis, ichthyosis, and deafness: multisystem effects of lethal GJB2 mutations. *J Am Acad Dermatol*. 2019;80(3):617–625.
26 Gilliam A, Williams ML. Fatal septicemia in an infant with keratitis, ichthyosis, and deafness (KID) syndrome. *Pediatr Dermatol*. 2002;19(3):232–236.
27 Griffith AJ, Yang Y, Pryor SP, et al. Cochleosaccular dysplasia associated with a connexin 26 mutation in keratitis-ichthyosis-deafness syndrome. *Laryngoscope*. 2006;116(8):1404–1408.
28 Janecke AR, Hennies HC, Gunther B, et al. GJB2 mutations in keratitis-ichthyosis-deafness syndrome including its fatal form. *Am J Med Genet*. 2005;133A(2):128–131.
29 Jonard L, Feldmann D, Parsy C, et al. A familial case of Keratitis-Ichthyosis-Deafness (KID) syndrome with the GJB2 mutation G45E. *Eur J Med Genet*. 2008;51(1):35–43.
30 Sbidian E, Feldmann D, Bengoa J, et al. Germline mosaicism in keratitis-ichthyosis-deafness syndrome: pre-natal diagnosis in a familial lethal form. *Clin Genet*. 2010;77(6):587–592.
31 Xu L, Carrer A, Zonta F, et al. Design and characterization of a human monoclonal antibody that modulates mutant connexin 26 hemichannels implicated in deafness and skin disorders. *Front Mol Neurosci*. 2017;10:298.
32 Ziraldo G, Buratto D, Kuang Y, et al. A human-derived monoclonal antibody targeting extracellular connexin domain selectively modulates hemichannel function. *Front Physiol*. 2019;10:392.
33 Nardin C, Tettey-Matey A, Donati V, et al. A quantitative assay for Ca2+ uptake through normal and pathological hemichannels. *Int J Mol Sci*. 2022;23(13):7337.
34 Kuang Y, Zorzi V, Buratto D, et al. A potent antagonist antibody targeting connexin hemichannels alleviates Clouston syndrome symptoms in mutant mice. *EBioMedicine*. 2020;57:102825.
35 Buratto D, Donati V, Zonta F, Mammano F. Harnessing the therapeutic potential of antibodies targeting connexin hemichannels. *Biochim Biophys Mol Basis Dis*. 2021;1867(4):166047.
36 Sasaki-Iwaoka H, Taguchi K, Okada Y, et al. AS2762900-00, a potent anti-human IL-23 receptor monoclonal antibody, prevents epidermal hyperplasia in a psoriatic human skin xenograft model. *Eur J Pharmacol*. 2019;843:190–198.
37 Kopecki Z, Ruzehaji N, Turner C, et al. Topically applied flightless I neutralizing antibodies improve healing of blistered skin in a murine model of epidermolysis bullosa acquisita. *J Invest Dermatol*. 2013;133(4):1008–1016.

38 Fang J, Qian JJ, Yi S, et al. Stable antibody expression at therapeutic levels using the 2A peptide. *Nat Biotechnol*. 2005;23(5):584–590.
39 Hollevoet K, Declerck PJ. State of play and clinical prospects of antibody gene transfer. *J Transl Med*. 2017;15(1):131.
40 Patel A, Bah MA, Weiner DB. In Vivo delivery of nucleic acid-encoded monoclonal antibodies. *BioDrugs*. 2020;34(3):273–293.
41 Mese G, Sellitto C, Li L, et al. The Cx26-G45E mutation displays increased hemichannel activity in a mouse model of the lethal form of keratitis-ichthyosis-deafness syndrome. *Mol Biol Cell*. 2011;22(24):4776–4786.
42 Sellitto C, Li L, White TW. Connexin hemichannel inhibition ameliorates epidermal pathology in a mouse model of keratitis ichthyosis deafness syndrome. *Sci Rep*. 2021;11(1):24118.
43 Kilkenny C, Browne WJ, Cuthill IC, Emerson M, Altman DG. Improving bioscience research reporting: the ARRIVE guidelines for reporting animal research. *PLoS Biol*. 2010;8(6):e1000412.
44 Smith AJ, Clutton RE, Lilley E, Hansen KEA, Brattelid T. PREPARE: guidelines for planning animal research and testing. *Lab Anim*. 2018;52(2):135–141.
45 McCafferty J, Griffiths AD, Winter G, Chiswell DJ. Phage antibodies: filamentous phage displaying antibody variable domains. *Nature*. 1990;348(6301):552–554.
46 Perisic O, Webb PA, Holliger P, Winter G, Williams RL. Crystal structure of a diabody, a bivalent antibody fragment. *Structure*. 1994;2(12):1217–1226.
47 Bujak E, Matasci M, Neri D, Wulhfard S. Reformatting of scFv antibodies into the scFv-Fc format and their downstream purification. *Methods Mol Biol*. 2014;1131:315–334.
48 Li C, Samulski RJ. Engineering adeno-associated virus vectors for gene therapy. *Nat Rev Genet*. 2020;21(4):255–272.
49 Engvall E, Perlmann P. Enzyme-linked immunosorbent assay, Elisa. 3. Quantitation of specific antibodies by enzyme-labeled anti-immunoglobulin in antigen-coated tubes. *J Immunol*. 1972;109(1):129–135.
50 Vogiatzis S, Celestino M, Trevisan M, et al. Lentiviral vectors expressing chimeric NEDD4 ubiquitin ligases: an innovative approach for interfering with alpha-synuclein accumulation. *Cells*. 2021;10(11):3256.
51 Nardin C, Peres C, Putti S, et al. Connexin hemichannel activation by S-nitrosoglutathione synergizes strongly with photodynamic therapy potentiating anti-tumor bystander killing. *Cancers*. 2021;13(20).
52 Donati V, Peres C, Nardin C, et al. Calcium signaling in the photodamaged skin: in vivo experiments and mathematical modeling. *Function*. 2022;3(1):zqab064.
53 Fuochi S, Rigamonti M, Iannello F, et al. Phenotyping spontaneous locomotor activity in inbred and outbred mouse strains by using Digital Ventilated Cages. *Lab Anim (NY)*. 2021;50(8):215–223.
54 Iannello F. Non-intrusive high throughput automated data collection from the home cage. *Heliyon*. 2019;5(4):e01454.
55 Au A, Shao Q, White KK, et al. Comparative analysis of Cx31 and Cx43 in differentiation-competent rodent keratinocytes. *Biomolecules*. 2020;10(10).
56 Tudor D, Chaudry F, Harper L, Mackenzie IC. The in vitro behaviour and patterns of colony formation of murine epithelial stem cells. *Cell Prolif*. 2007;40(5):706–720.
57 Badu-Nkansah KA, Lechler T. Proteomic analysis of desmosomes reveals novel components required for epidermal integrity. *Mol Biol Cell*. 2020;31(11):1140–1153.
58 Fallah M, Viklund E, Bäckman A, et al. Plasminogen is a master regulator and a potential drug candidate for the healing of radiation wounds. *Cell Death Dis*. 2020;11(3):201.
59 Sachs N, Secades P, van Hulst L, Kreft M, Song JY, Sonnenberg A. Loss of integrin alpha3 prevents skin tumor formation by promoting epidermal turnover and depletion of slow-cycling cells. *Proc Nat Acad Sci U S A*. 2012;109(52):21468–21473.
60 Siriwach R, Ngo AQ, Higuchi M, et al. Single-cell RNA sequencing identifies a migratory keratinocyte subpopulation expressing THBS1 in epidermal wound healing. *iScience*. 2022;25(4):104130.
61 Cardiff RD, Miller CH, Munn RJ. Manual hematoxylin and eosin staining of mouse tissue sections. *Cold Spring Harb Protoc*. 2014;2014(6):655–658.
62 Kim JY, Ash RT, Ceballos-Diaz C, et al. Viral transduction of the neonatal brain delivers controllable genetic mosaicism for visualising and manipulating neuronal circuits in vivo. *Eur J Neurosci*. 2013;37(8):1203–1220.
63 Mauro VP, Chappell SA. A critical analysis of codon optimization in human therapeutics. *Trends Mol Med*. 2014;20(11):604–613.
64 Alexopoulou AN, Couchman JR, Whiteford JR. The CMV early enhancer/chicken beta actin (CAG) promoter can be used to drive transgene expression during the differentiation of murine embryonic stem cells into vascular progenitors. *BMC Cell Biol*. 2008;9:2.
65 Cantore A, Ranzani M, Bartholomae CC, et al. Liver-directed lentiviral gene therapy in a dog model of hemophilia B. *Sci Transl Med*. 2015;7(277):277ra28.
66 Naldini L. Gene therapy returns to centre stage. *Nature*. 2015;526(7573):351–360.
67 Koster MI. Making an epidermis. *Ann N Y Acad Sci*. 2009;1170:7–10.
68 Fuchs E. Chapter nineteen - epithelial skin Biology: three decades of developmental Biology, a hundred questions answered and a thousand new ones to address. In: Wassarman PM, ed. *Current topics in developmental Biology*. Academic Press; 2016:357–374.
69 Boukamp P, Petrussevska RT, Breitkreutz D, Hornung J, Markham A, Fusenig NE. Normal keratinization in a spontaneously immortalized aneuploid human keratinocyte cell line. *J Cell Biol*. 1988;106(3):761–771.
70 Johnson RG, Le HC, Evenson K, et al. Connexin hemichannels: methods for dye uptake and leakage. *J Membr Biol*. 2016;249(6):713–741.
71 Tucci MG, Offidani A, Lucarini G, et al. Advances in the understanding of malignant transformation of keratinocytes: an immunohistochemical study. *J Eur Acad Dermatol Venereol : JEADV*. 1998;10(2):118–124.
72 Toivola DM, Boor P, Alam C, Strnad P. Keratins in health and disease. *Curr Opin Cell Biol*. 2015;32:73–81.
73 Zhang X, Yin M, Zhang LJ. Keratin 6, 16 and 17-critical barrier alarmin molecules in skin wounds and psoriasis. *Cells*. 2019;8(8).
74 Riquelme MA, Kar R, Gu S, Jiang JX. Antibodies targeting extracellular domain of connexins for studies of hemichannels. *Neuropharmacology*. 2013;75:525–532.
75 Goertsen D, Flytzanis NC, Goeden N, et al. AAV capsid variants with brain-wide transgene expression and decreased liver targeting after intravenous delivery in mouse and marmoset. *Nat Neurosci*. 2022;25(1):106–115.
76 Giaume C, Naus CC, Saez JC, Leybaert L. Glial connexins and pannexins in the healthy and diseased brain. *Physiol Rev*. 2021;101(1):93–145.
77 Cammarata-Scalisi F, Willoughby CE, Cardenas Tadich A, Labrador N, Herrera A, Callea M. Clinical, etiopathogenic, and therapeutic aspects of KID syndrome. *Dermatol Ther*. 2020;33(4):e13507.
78 Patel V, Sun G, Dickman M, Khuu P, Teng JM. Treatment of keratitis-ichthyosis- deafness (KID) syndrome in children: a case report and review of the literature. *Dermatol Ther*. 2015;28(2):89–93.
79 Bosen F, Schutz M, Beinhauer A, Strenzke N, Franz T, Willecke K. The Clouston syndrome mutation connexin30 A88V leads to hyperproliferation of sebaceous glands and hearing impairments in mice. *FEBS Lett*. 2014;588(9):1795–1801.
80 Essenfelder GM, Bruzzone R, Lamartine J, et al. Connexin30 mutations responsible for hidrotic ectodermal dysplasia cause abnormal hemichannel activity. *Hum Mol Genet*. 2004;13(16):1703–1714.
81 Au HKE, Isalan M, Mielcarek M. Gene therapy advances: a meta-analysis of AAV usage in clinical settings. *Front Med*. 2022;8.
82 Colella P, Sellier P, Costa Verdera H, et al. AAV gene transfer with tandem promoter design prevents anti-transgene immunity and provides persistent efficacy in neonate pompe mice. *Mol Ther Methods Clin Dev*. 2019;12:85–101.
83 Becker J, Fakhiri J, Grimm D. Fantastic AAV gene therapy vectors and how to find them-random diversification, rational design and machine learning. *Pathogens*. 2022;11(7).
84 Mullard A. FDA approves 100th monoclonal antibody product. *Nat Rev Drug Discov*. 2021;20(7):491–495.
85 Yeo JHM, Mariati Yang Y. An IRES-mediated tricistronic vector for efficient generation of stable, high-level monoclonal antibody producing CHO DG44 cell lines. *Methods Mol Biol*. 2018;1827:335–349.
86 Fishman JB, Berg EA. Antibody purification and storage. *Cold Spring Harb Protoc*. 2019;2019(5).
87 Chiodin D, Cox EM, Edmund AV, Kratz E, Lockwood SH. Regulatory affairs 101: introduction to investigational new drug applications and clinical trial applications. *Clin Transl Sci*. 2019;12(4):334–342.
88 Schalper KA, Palacios-Prado N, Retamal MA, Shoji KF, Martinez AD, Saez JC. Connexin hemichannel composition determines the

FGF-1-induced membrane permeability and free [Ca2+]i responses. *Mol Biol Cell*. 2008;19(8):3501–3513.
89 Schalper KA, Sanchez HA, Lee SC, Altenberg GA, Nathanson MH, Saez JC. Connexin 43 hemichannels mediate the Ca2+ influx induced by extracellular alkalinization. *Am J Physiol Cell Physiol*. 2010;299(6):C1504–C1515.
90 Fiori MC, Figueroa V, Zoghbi ME, Saez JC, Reuss L, Altenberg GA. Permeation of calcium through purified connexin 26 hemichannels. *J Biol Chem*. 2012;287(48):40826–40834.
91 Sanchez HA, Orellana JA, Verselis VK, Saez JC. Metabolic inhibition increases activity of connexin-32 hemichannels permeable to Ca2+ in transfected HeLa cells. *Am J Physiol Cell Physiol*. 2009;297(3):C665–C678.
92 Mandal A, Shahidullah M, Delamere NA. Calcium entry via connexin hemichannels in lens epithelium. *Exp Eye Res*. 2015;132:52–58.
93 Cotrina ML, Lin JH, Alves-Rodrigues A, et al. Connexins regulate calcium signaling by controlling ATP release. *Proc Nat Acad Sci U S A*. 1998;95(26):15735–15740.
94 Stout CE, Costantin JL, Naus CC, Charles AC. Intercellular calcium signaling in astrocytes via ATP release through connexin hemichannels. *J Biol Chem*. 2002;277(12):10482–10488.
95 Pearson RA, Dale N, Llaudet E, Mobbs P. ATP released via gap junction hemichannels from the pigment epithelium regulates neural retinal progenitor proliferation. *Neuron*. 2005;46(5):731–744.
96 Anselmi F, Hernandez VH, Crispino G, et al. ATP release through connexin hemichannels and gap junction transfer of second messengers propagate Ca2+ signals across the inner ear. *Proc Nat Acad Sci U S A*. 2008;105(48):18770–18775.
97 Mazzarda F, D'Elia A, Massari R, et al. Organ-on-chip model shows that ATP release through connexin hemichannels drives spontaneous Ca(2+) signaling in non-sensory cells of the greater epithelial ridge in the developing cochlea. *Lab Chip*. 2020;20(16):3011–3023.
98 Burnstock G, Knight GE, Greig AV. Purinergic signaling in healthy and diseased skin. *J Invest Dermatol*. 2012;132(3 Pt 1):526–546.
99 Peng B, Xu C, Wang S, Zhang Y, Li W. The role of connexin hemichannels in inflammatory diseases. *Biology*. 2022;11(2).
100 Decrock E, Vinken M, De Vuyst E, et al. Connexin-related signaling in cell death: to live or let die? *Cell Death Differ*. 2009;16(4):524–536.
101 Chandrasekhar A, Bera AK. Hemichannels: permeants and their effect on development, physiology and death. *Cell Biochem Funct*. 2012;30(2):89–100.
102 Vinken M. Connexin hemichannels: novel mediators of toxicity. *Arch Toxicol*. 2015;89(1):143–145.
103 Elias P, Ahn S, Brown B, Crumrine D, Feingold KR. Origin of the epidermal calcium gradient: regulation by barrier status and role of active vs passive mechanisms. *J Invest Dermatol*. 2002;119(6):1269–1274.
104 Elias PM, Ahn SK, Denda M, et al. Modulations in epidermal calcium regulate the expression of differentiation-specific markers. *J Invest Dermatol*. 2002;119(5):1128–1136.
105 Lee SE, Lee SH. Skin barrier and calcium. *Ann Dermatol*. 2018;30(3):265–275.
106 Inoue M. Genetically encoded calcium indicators to probe complex brain circuit dynamics in vivo. *Neurosci Res*. 2021;169:2–8.
107 White D, Yang Q. Genetically encoded ATP biosensors for direct monitoring of cellular ATP dynamics. *Cells*. 2022;11(12):1920.
108 Srinivas M, Jannace TF, Cocozzelli AG, et al. Connexin43 mutations linked to skin disease have augmented hemichannel activity. *Sci Rep*. 2019;9(1):19.
109 Wang H, Cao X, Lin Z, et al. Exome sequencing reveals mutation in GJA1 as a cause of keratoderma-hypotrichosis-leukonychia totalis syndrome. *Hum Mol Genet*. 2015;24(1):243–250.